Ocean Dynamics (2006) 56: 543–567
DOI 10.1007/s10236-006-0082-1

Barnier Bernard · Gurvan Madec · Thierry Penduff · Jean-Marc Molines · Anne-Marie Treguier · Julien Le Sommer · Aike Beckmann · Arne Biastoch · Claus Böning · Joachim Dengg · Corine Derval · Edmée Durand · Sergei Gulev · Elizabeth Remy · Claude Talandier · Sébastien Theetten · Mathew Maltrud · Julie McClean · Beverly De Cuevas

Impact of partial steps and momentum advection schemes in a global ocean circulation model at eddy-permitting resolution

Received: 2 September 2005 / Accepted: 22 March 2006 / Published online: 14 June 2006

Abstract Series of sensitivity tests were performed with a *z*-coordinate, global eddy-permitting (1/4°) ocean/sea-ice model (the ORCA-R025 model configuration developed for the DRAKKAR project) to carefully evaluate the impact of recent state-of-the-art numerical schemes on model solutions. The combination of an energy–enstrophy conserving (*EEN*) scheme for momentum advection with a partial step (*PS*) representation of the bottom topography yields significant improvements in the mean circulation. Well known biases in the representation of western boundary currents, such as in the Atlantic the detachment of the Gulf Stream, the path of the North Atlantic Current, the location of the Confluence, and the strength of the Zapiola Eddy in the south Atlantic, are partly corrected. Similar improvements are found in the Pacific, Indian, and Southern Oceans, and characteristics of the mean flow are generally much closer to observations. Comparisons with other state-of-the-art models show that the ORCA-R025 configuration generally performs better at similar resolution. In addition, the model solution is often comparable to solutions obtained at 1/6 or 1/10° resolution in some aspects concerning mean flow patterns and distribution of eddy kinetic energy. Although the reasons for these improvements are not analyzed in detail in this paper, evidence is shown that the combination of EEN with PS reduces numerical noise near the bottom, which is likely to affect current–topography interactions in a systematic way. We conclude that significant corrections of the mean biases presently seen in general circulation model solutions at eddy-permitting resolution can still be expected from the development of numerical methods, which represent an alternative to increasing resolution.

Keywords Global ocean · Eddy-permitting ocean model · Momentum advection scheme · Partial step topography · Eddy/topography interactions

Responsible editor: Lee-Lueng Fu

B. Bernard (✉) · T. Penduff · J.-M. Molines · J. Le Sommer
Laboratoire des Ecoulements Géophysiques et Industriels,
Grenoble, France
e-mail: bernard.barnier@hmg.inpg.fr

G. Madec · C. Talandier
Laboratoire d'Océanographie Dynamique et de Climatologie,
Paris, France

A.-M. Treguier · S. Theetten
Laboratoire de Physique des Océans, Ifremer Centre de Brest,
Plouzané, France

A. Beckmann
Department of Physical Sciences, Division of Geophysics,
University of Helsinki,
Helsinki, Finland

A. Biastoch · C. Böning · J. Dengg
IfM-GEOMAR, Leibniz-Institut für Meereswissenschaften an der Universität Kiel,
Kiel, Germany

C. Derval · E. Durand · E. Remy
MERCATOR-Ocean,
Toulouse, France

S. Gulev
Shirshov Institut of Oceanography,
Russian Academy of Science,
Moscow, Russia

M. Maltrud
Fluid Dynamics Group, Los Alamos National Laboratory,
Los Alamos, USA

J. McClean
Scripps Institution of Oceanography, UCSD,
LA Jolla, USA

B. De Cuevas
National Oceanography Centre,
Southampton, UK

1 Introduction

In a special issue honoring the memory of Christian Le Provost, it is fitting for many of us who collaborated with him, sometimes very closely and for almost 20 years, to place the work presented here in relation to scientific

issues he stood by. Christian Le Provost's first involvement in the field of ocean circulation modeling was motivated by the World Ocean Circulation Experiment (WOCE) in the mideighties. His intuition was that among all processes which have a crucial influence in shaping the mean circulation, two of particular importance were overlooked: the mesoscale eddies and the constraint of the bottom topography. His early work therefore concentrated on process studies searching for a better understanding and modeling of the generation of eddies in the presence of topography (Verron and Le Provost 1985; Verron et al. 1987) and the interaction of turbulent large-scale flows with topography (Barnier and Le Provost 1993). He also emphasized the crucial importance of numerics on the realism of model solutions (Blayo and Le Provost 1993). Christian convinced himself and his group that accurate modeling of the effect of bottom topography on ocean nonlinear flows is a key to achieve realistic simulations of the global ocean circulation. This belief underlay the model intercomparison DYNAMO project (DYNAMO Group 1997), which he designed with Jürgen Willebrand (Willebrand et al. 2001).

Building and running ocean models able to simulate the world ocean circulation with great realism require a great variety of scientific skills. Christian Le Provost was aware that gathering all the necessary skills within a single research team as the one he was leading would be difficult. Consequently, he always favored community experiments in the spirit of the Community Model Experiment carried out under WOCE (Bryan and Holland 1989; Böning and Bryan 1996). This concept of community projects, which Christian shared with Jürgen Willebrand, Bill Holland, and others, was at the core of the DYNAMO project. It was at the origin of the French CLIPPER project (Treguier et al. 1999) and is the basis of the international DRAKKAR project, which is briefly presented here. These are projects in which Christian Le Provost actively participated.

The present paper is strongly inspired by the issues mentioned above. It presents recent advances in modeling the general ocean circulation at eddy-permitting resolution achieved in the framework of the European modeling project DRAKKAR. Indeed, eddy-permitting models are still worth exploring and enhancing, despite the existing higher resolution models because they will be the target resolution of the next generation of climate models. Improvements presented here mainly concern the representation of ocean flows in regions where the circulation is dominated by nonlinearities and is strongly constrained by bottom topography. These results were obtained by using a new numerical treatment of the nonlinear advection term in momentum equations and a partial step representation of the bottom topography.

The paper is organized as follows. Section 2 describes the eddy-permitting, global, 1/4° model configuration implemented by the project, ORCA-R025. It also presents the mean circulation produced by ORCA-R025 under a climatological atmospheric forcing. Section 3 evaluates the impact of new numerical choices regarding bottom topography and momentum, in direct relation with Christian Le Provost early intuition, by comparison of ORCA-R025 simulations with observations and other state-of-the-art model simulations at equivalent or higher resolution. Section 4 identifies key issues where problems remain and ways of improving.

2 Global 1/4° DRAKKAR configuration ORCA-R025

2.1 DRAKKAR project

During the last decade, scientists participating in the DRAKKAR[1] project fostered cooperative activities within the European project DYNAMO (Dynamics of North Atlantic Models, DYNAMO Group 1997) and between their respective national projects, CLIPPER in France (Treguier et al. 1999) and FLAME (Family of Linked Atlantic models) in Germany (Böning et al. 2003). The challenge of developing realistic global ocean models suited for a wide range of applications will be better met with an effective integration and coordination of activities and complementary expertises of the groups. This yielded the DRAKKAR concept, a European modeling project, which provides the framework for joint and coordinated modeling studies between research groups in France, Germany, Russia, and Finland.

One primary concern of the project is related to the circulation and variability in the North Atlantic Ocean as driven by the atmospheric forcing, by interactions between processes of different scales, by exchanges between basins and regional circulation features (including the Nordic Seas), and by the influence of the world ocean circulation (including the Arctic and Southern Oceans and the Agulhas retroflection region). To achieve these scientific objectives, DRAKKAR is carrying out coordinated realistic simulations of the ocean circulation at regional and global scales with pertinent atmospheric forcing and resolutions high enough to ensure physical consistency over the range of scales which are dynamically important (i.e., from eddy to global and from day to decade).

For its first objective, the project has built a hierarchy of numerical model configurations from global to regional scale, each based on the NEMO[2] modeling system, which presently includes the latest version of the primitive equation, free surface (Roullet and Madec 2000) ocean circulation code OPA9 (Madec et al. 1998) coupled to the multilayered sea-ice code LIM2 (Fichefet et al. 1997). This hierarchy of models includes the ORCA-R025 configuration, an eddy-permitting, global ocean/sea-ice configuration with a resolution of 1/4° described below.

[1] http://www.ifremer.fr/lpo/drakkar.

[2] NEMO: Nucleus for European Models of the Ocean.

2.2 Global 1/4° DRAKKAR configuration ORCA-R025

2.2.1 ORCA grid common to all DRAKKAR configurations

In the OPA numerical code (Madec et al. 1998), the primitive equations are discretized on a C-grid centered at tracer points. A family of tripolar grids, ORCA grids, was developed by Madec (personal communication) for global models (see Timmmerman et al. 2005 for an application of the ORCA grid at 2° resolution). The geographical South Pole is conserved and from 80°S to 20°N, the grid is a regular Mercator grid (isotropic, getting finer at high latitude as the cosine of latitude). Following Murray's (1996) idea, the singularity of the North Pole is treated by changing the coordinate system using two poles, one in Canada and the other in Asia. Starting at 20°N, latitude circles of the Mercator grid are progressively distorted into ellipses, the great axes of which are oriented along a line joining the two poles of the northern hemisphere. The grid is computed following the semianalytical method of Madec and Imbard (1996). The deformation of the grid is such that it remains quasi-isotropic and is quasi-uniform in the Arctic. Because the resolution of the grid is variable, the resolution of an ORCA grid is referred to the latitude of the equator where it is the coarsest. This family of grid is used for all DRAKKAR configurations, including the regional ones (North Atlantic and Nordic Seas).

2.2.2 Model grid, bathymetry, and initial conditions

ORCA-R025 is a global configuration of NEMO implemented on an ORCA grid at 1/4° resolution. Grid, masking, and initial conditions are inherited from the global configuration of the operational oceanography center MERCATOR-Ocean[3] (Remy et al., personal communication). This configuration has 1,442×1,021 grid points and uses 46 vertical levels. Vertical grid spacing is finer near the surface (6 m) and increases with depth to 250 m at the bottom. The maximum depth in the model is 5,844 m. The effective resolution, which gets finer with increasing latitudes, is ~27.75 km at the equator and ~13.8 km at 60°S or 60°N. It gets to ~7 km in the Weddell and Ross Seas and ~10 km in the Arctic.

The bathymetry is derived from the 2-min resolution Etopo2 bathymetry file of National Geophysical Data Center, which is a combination of the satellite-based bathymetry (Smith and Sandwell (1997) and International Bathymetric Chart of the Arctic Ocean (Jakobsson et al. 2000). It was merged with the Bedrock Mapping Project data (Lythe and Vaughan 2001) beyond 72°S in the Antarctic. The interpolation onto the model grid was carried out by taking all the Etopo2 grid points falling into an ORCA-R025 grid box and taking the median of those points. This produces a smoothing of the subgrid scale topography. Penduff et al. (2002) showed that topographic smoothing has a strong influence on the model's circulation. We believe that topography should not vary too much at the grid scale to avoid numerical noise. For this reason, we have applied an additional smoothing (two passes of a uniform shapiro filter). Hand editing was performed in a few key areas. Initial conditions for temperature and salinity are derived from the Levitus et al. (1998) data set for the middle and low latitudes. For high latitudes, we chose the PHC2.1 climatology (Steele et al. 2001) and for the Mediterranean Sea, the Medatlas climatology (Jourdan et al. 1998).

2.2.3 Numerical characteristics

A purpose of developing the NEMO code is to improve model physics and numerical algorithms. Perhaps the most significant problem in eddy-permitting *z*-coordinate ocean models is the misrepresentation of flow–topography interactions (Penduff et al. 2005). The previous version of OPA (OPA 8.1, Madec et al. 1998) represented the topography as staircases whose steps have the size of the model vertical levels: This is the "full step" (*FS*) topography, which approximates the true ocean depth to the closest model level. By making the depth of the bottom cell variable and adjustable to the real depth of the ocean, it is possible to better represent small topographic slopes: This is the "partial step" (*PS*) topography, first introduced by Adcroft et al. (1997) and also named partial cells in the literature (Pacanowski and Gnanadesikan 1998). This PS representation of the topography is now available in NEMO.

In OPA, the momentum equations are expressed in their vector invariant formulation (i.e., as a relative vorticity term plus a gradient of kinetic energy and a vertical advection) instead of the flux form (i.e., divergence of momentum fluxes plus a metric term) used in most ocean general circulation models. At this point, several options are possible to discretize the total (relative + planetary) vorticity term. Two distinct schemes are used in the present paper. One is the standard scheme used in the former versions of OPA (referred to as the *ENS* scheme) and has the property to conserve enstrophy (Sadourny 1975) in flows with no mass flux divergence. The other, which is newly available in NEMO, is an adaptation of the scheme of Arakawa and Lamb (1981) to the primitive equations. Referred to as the energy–enstrophy conserving (*EEN*) scheme, it conserves total energy for general flow and potential enstrophy for flows with no mass flux divergence. These two new options (PS + EEN) have a drastic impact on the model solution as will be demonstrated in Section 3.

Other options worth noting in ORCA-R025 and all DRAKKAR configurations are: (1) a total variance diminishing advection scheme for tracers (Lévy et al. 2001), which, compared to the centered scheme, avoids the generation of overshoots in case of sharp gradients; (2) a Laplacian lateral isopycnal diffusion on tracers (300 m^2 s^{-1} at the equator and decreasing poleward, proportionally to

[3] MERCATOR-Ocean: http://www.mercator-ocean.fr.

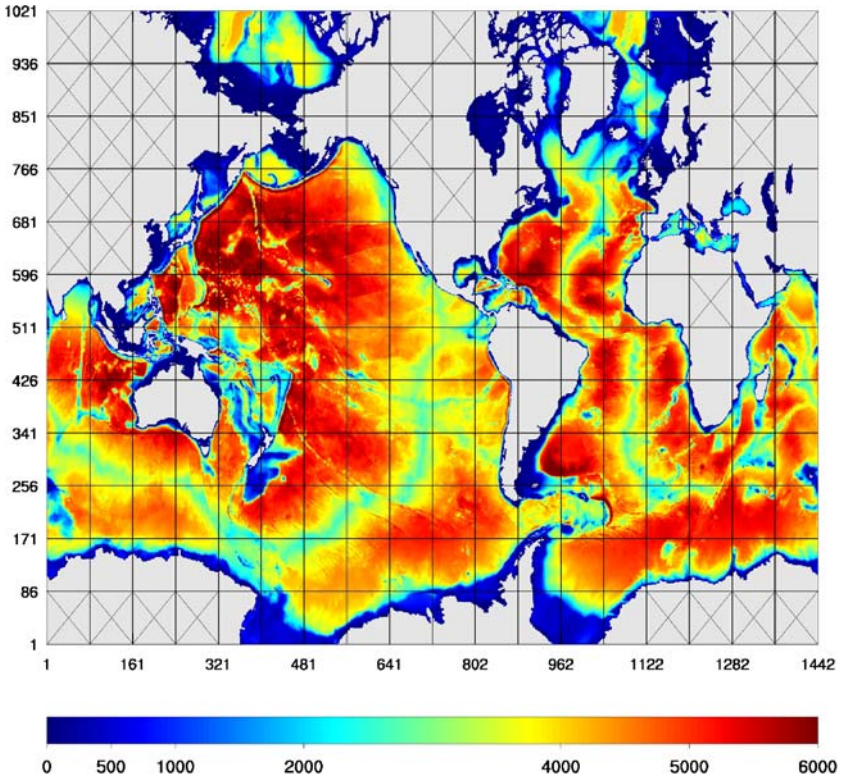

Fig. 1 Domain decomposition on 186 processors of the DRAKKAR global 1/4° ocean circulation model ORCA-R025. *Colors* indicate the model bathymetry in meters. Every single *box* represents the domain accounted for by a processor. *Boxes with a cross* are "land processors" not retained in the calculation. *Numbers* in abscissa and ordinate indicate model grid points

the grid size); and (3) a horizontal biharmonic viscosity for momentum (-1.5×10^{11} m^4 s^{-1} at the equator and decreasing poleward as the cube of the grid size). In the equatorial waveguide, a Laplacian viscosity (500 m^2 s^{-1}) is added to the biharmonic operator at levels included in the upper 100 m to better control the speed of the Equatorial Undercurrent. This method gave satisfying results in the CLIPPER model (M. Arhan et al. 2006, in revision).

Surface boundary layer mixing and interior vertical mixing are parameterized according to a turbulent closure model (order 1.5) adapted to OPA by Blanke and Delecluse (1993). In case of static instability, a viscosity/diffusivity enhancement up to 10 m^2 s^{-1} is used.

2.2.4 Forcing

The atmospheric forcing, which drives the simulations presented here, is a climatological seasonal cycle forcing applied in a cycling way. It is the same forcing used by Timmermann et al. (2005) in their application of older versions of OPA and LIM at coarser resolution (2°), except for the wind forcing, which here, uses European Space Agency remote sensing satellite (ERS) scatterometer winds.

Surface momentum flux is directly provided to the ocean/sea-ice model as a wind stress vector. A climatological daily mean wind stress vector is used. It is a combination of ERS scatterometer data (CERSAT 2002) and National Centers for Environmental Prediction/National Center for Atmospheric Research (NCEP/NCAR) reanalysis (Kalnay et al. 1996) built as follows: ERS wind stress between 50°N and 50°S, a linear combination of ERS winds with NCEP between 50°and 60°, and NCEP winds poleward of 60°. The daily climatology is built using years 1992 to 2000 with an 11-day running mean filter to remove synoptic variability.

Surface heat fluxes (solar, infrared, latent, and sensible heat) and freshwater flux for ocean and sea-ice are calculated using the empirical bulk parameterization described by Goosse (1997). Evaporation is derived from the latent heat flux. The set of atmospheric variables used in these flux calculations consists of climatological daily mean values of air temperature from NCEP/NCAR reanalysis, climatological monthly mean precipitation from CMAP (Xie and Arkin 1997), monthly mean humidity (Trenberth et al. 1989) and cloud cover (Berliand and Strokina 1980), and climatological daily mean wind speed from the blend of ERS and NCEP/NCAR reanalysis described above. River runoff was provided by MERCATOR-Ocean (Remy, personal communication). No relaxation to any sea surface temperature or sea surface salinity (*SSS*) is used.

2.2.5 Performance

ORCA-R025 is implemented on a massively parallel machine at IDRIS.[4] We applied a domain decomposition technique and split the global computational domain into 18×12 subdomains (216 in all). To streamline efficiency,

[4] Institut du Développement et des Ressources en Informatique Scientifique, Orsay, France.

Table 1 List of the 10-year-long sensitivity experiments carried out with ORCA-R025

Simulation	Vorticity scheme	Bottom topography*
G03	EEN (new)	FS
G04	ENS (old)	FS
G22	EEN (new)	PS

The present study mainly uses the results from the G04 and G22 simulations. No relaxation to SSS is applied in any of these experiments. A free slip sidewall boundary condition is used in all simulations

**FS* Full step and *PS* partial step

we used only processors having ocean grid points (186 processors). Each processor thus had 82×87×46 grid points. A one-row overlapping halo (1 row) is shared with the neighboring processors, using explicit communications between processors, (Message Passing Interface library). Figure 1 gives a global view of the domain broken-down into individual processors. The time step of the ocean component is 1,440 s (60 time steps per day) and the sea-ice component is called once every five time steps. One year of model simulation requires 2,200 h of CPU on 186 IBM SP4 processors and takes about 12.6 h of elapsed time. Maximum memory is 0.479 Gb per processor and total memory is 84 Gb.

2.3 Sensitivity tests with ORCA-R025

A series of 10-year simulations were run to evaluate the contribution of various numerical choices to the solution. The focus is on the *PS representation of topography* and the *EEN vorticity scheme* used in the calculation of momentum advection, which produced the greatest improvements to the model solution. Therefore, we compare (in Section 3) a simulation that does not include these two features, referred to as G04, with a simulation that includes both, referred to as G22, (Table 1). Other numerical options were tested. In particular, a FS simulation using the EEN vorticity scheme was run (simulation G03, Table 1) so the effects of the PS could be separated. Some results from this experiment will be used in Section 3.

Before we provide (in Section 3) an assessment of the changes induced by the numerics, we provide a brief overview of simulation G22 (with PS and the EEN momentum advection scheme). Our analysis will remain rather descriptive. A full understanding of how the numerics impact on the physics of the model requires a large number of sensitivity experiments and complex diagnostics, which are currently under way in a North Atlantic configuration of the code (J. Le Sommer et al. 2006, in preparation). Preliminary results from this work are used in the discussion of Section 4 to illustrate possible

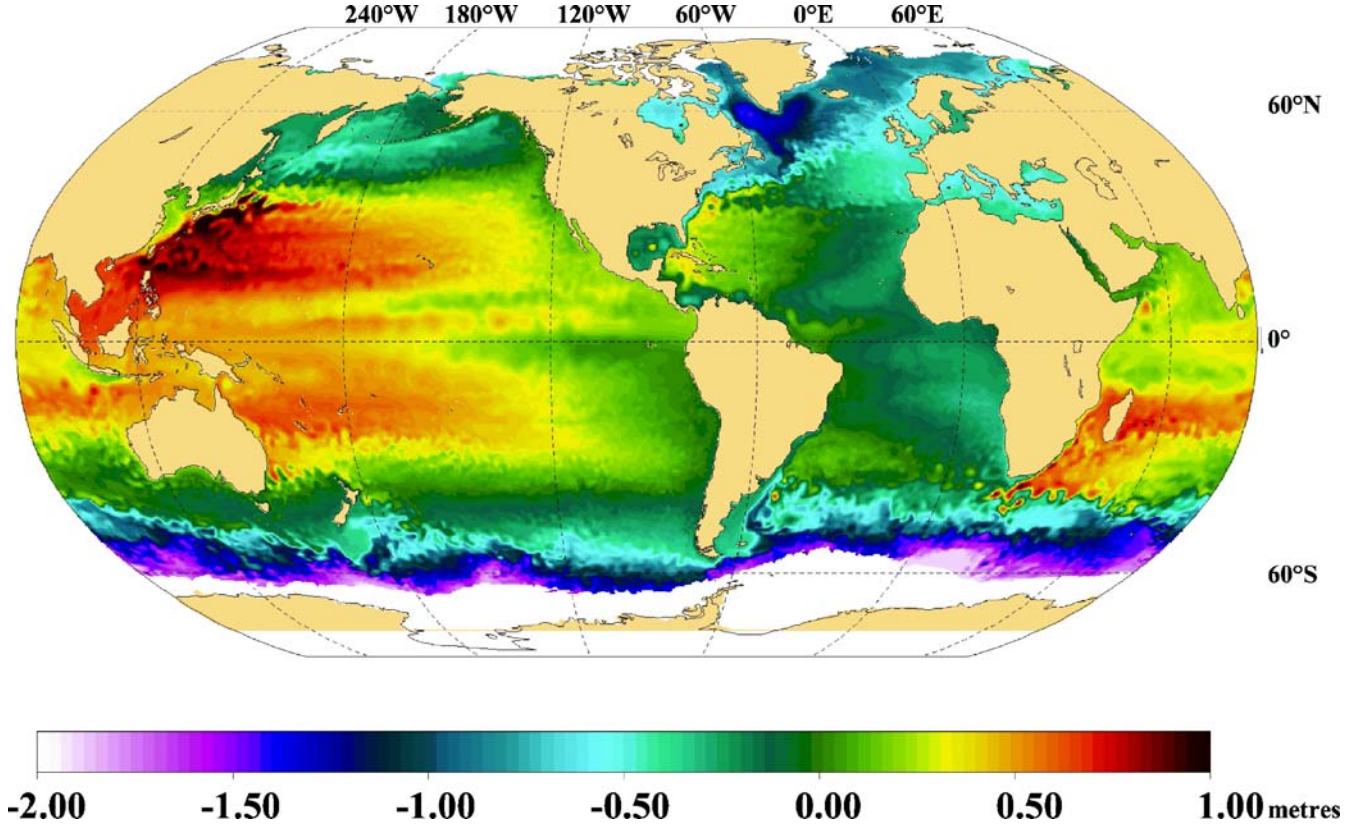

Fig. 2 Simulation G22 (partial step topography, new EEN vorticity scheme for momentum advection): snapshot of the sea surface height (*ssh*, in *color*) and ice cover (in *white*) in Austral winter in year 10 of the simulation

reasons of improvements when the combination PS + EEN is used.

2.4 Mean general circulation in simulation G22

2.4.1 Upper ocean circulation

A first overview of the large-scale upper circulation is presented in Fig. 2 with a snapshot of the sea surface height (*ssh*) and sea-ice cover in year 10 of the simulation. It shows the known general circulation features that are seen in similar model simulations (Maltrud et al. 1998; Maltrud and McClean 2005): the well-marked subpolar and subtropical gyres, the strong and meandering western boundary currents, the large upwelling systems of eastern ocean basins, and the equatorial current systems with waves and eddies. The strong Antarctic Circumpolar Current (ACC, almost a 2-m change in ssh) shows many mesoscale features. Agulhas Rings are drifting northwestward in the South Atlantic. Western boundary currents, the North Brazil Retroflection area, and the Caribbean Sea are rich in mesoscale features. Loop Current eddies are found in the Gulf of Mexico.

The distribution of the eddy kinetic energy (*eke*) compares remarkably well with the satellite estimate of Ducet et al. (2000) considering the medium resolution (1/4°) of the model (Fig. 5). There are regions where a significant improvement is found compared to other experiments (see next section). One is the Brazil–Malvinas Confluence Zone in the South Atlantic with the characteristic C-shape and the minimum of eke inside the Zapiola anticyclone (de Miranda et al. 1999a). Another is the Agulhas region where the paths of Agulhas Rings tend to be more realistic than in experiments with FS topography. The Gulf Stream and the North Atlantic Current system are also regions where the distribution pattern of eke is clearly improved, in particular, in the Northwest Corner. As shown in following sections, the distribution pattern of eke is sometimes better in simulation G22 than in 1/6° and even 1/10° experiments.

Sea-ice is not the focus of the present paper and only a quick overview is presented (the Austral winter sea-ice cover is shown in Fig. 2). A first look at the sea-ice component of simulation G22 shows reasonable performance in high latitudes. In the Arctic, the climatological winter sea-ice extent, area, and thickness are reproduced quite well with many small-scale details in the marginal ice zone present (e.g., ice tongues in the Greenland Sea, off Newfoundland, in the Okhotsk Sea, and partial coverage of the Baltic Sea). The summer ice distribution is characterized by a general overestimation of the ice cover. For the Antarctic Marginal Seas, we find larger differences between observed climatology and the model results. While the winter extent is acceptable, the thickness shows a systematic bias: too thick in all coastal regions and too thin offshore. The former leads to an overestimation in ice surviving the summer. Simulations with other global configurations of NEMO (at 1/2 and 2° resolutions) run within the DRAKKAR project show that this is a general feature of the coupled model system, not related specifically to the high-resolution case presented here. It will be investigated in more detail in a separate study.

2.4.2 Meridional circulation

The meridional overturning cell (MOC) or streamfunction and the meridional heat transport (MHT) provide a zonally averaged view of the meridional circulation. They are quantities of important climate relevance that ocean models aim to simulate accurately. In 10-year-long simulations as presented here, these quantities are still far from a state of equilibrium. However, they are systematically analyzed in similar model studies (Maltrud and McClean 2005; Lee and Coward 2003). An initial assessment of the strength of the meridional circulation in our model is useful because it characterizes the global dynamical regime in which simulations are compared.

We choose to comment on simulation G22 because it is representative of all three simulations in that respect, the MOC being very similar in simulations G03 and G04. Note that the simulations discussed here do not include a bottom boundary layer to improve the deep overflows, usually not reproduced well in *z*-coordinate models.

The MOC and MHT of G22 are shown in Figs. 3 and 4. It is very clear from Fig. 4 that the simulation is still far from equilibrium, as displayed by the large discrepancies between the advective MHT (i.e., estimated from correlation of the meridional velocity with the temperature) and the MHT diagnosed from the meridional integration of the surface fluxes (under the hypothesis of a state of equilibrium). These differences are indicative of significant trends in the model heat storage.

In the Atlantic, the maximum overturning is 24 Sv (Fig. 3a) with over 6 Sv of dense water overflow across the sills of the Nordic Seas. The MOC of G03 and G04 (not shown) are identical to that of G22 in that respect. These values are in the upper bounds of the values found in the literature, indicating a particularly strong meridional circulation in the northern North Atlantic under the present forcing conditions in all our simulations. The southward flow of North Atlantic Deep Water shows a significant decrease in the South Atlantic from 16 Sv at the equator to 9 Sv at 30°S. Northward flow of Antarctic Bottom Water is 4 Sv below 3,800 m. The maximum MHT is 1.28 PW at 28.5°N (Fig. 4a), a realistic value at this latitude. However, the MHT is generally weaker than the estimates obtained by an inversion of hydrographic sections by Ganachaud and Wunsch (2003). The comparison of the advective MHT with the MHT diagnosed from surface fluxes indicates a heat storage (i.e., warming) of the North Atlantic at latitudes higher than 30°S and a cooling elsewhere (between 30°S to 30°N). The model, therefore, is far from adjusted to the forcing field, limiting a quantitative interpretation of the above numbers.

In the Indo-Pacific, the MOC structure of G22 (Fig. 3b) and those of G034 and G04 (not shown) shows a relatively

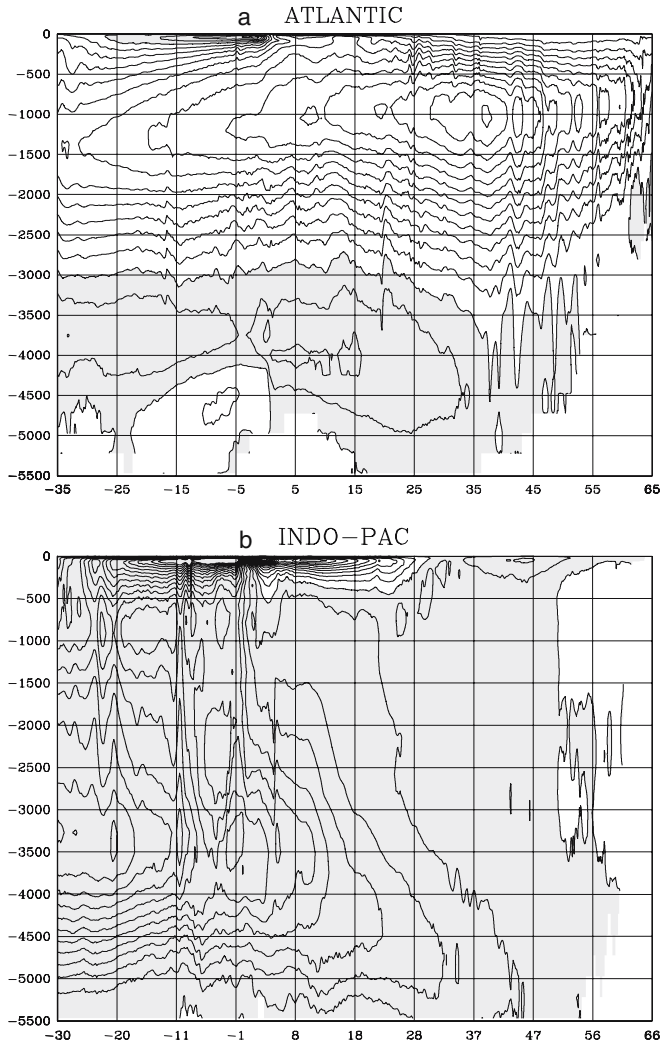

Fig. 3 Meridional overturning streamfunction (in Sv) averaged over year 8 to 10 of the G22 simulation (PS + EEN) for the Atlantic (**a**) and the Indo-Pacific ocean basins (**b**). Contour interval is 2 Sv

deep reaching shallow overturning cell; the equatorward subsurface flow, which compensates the poleward Ekman transport spreads down to 500 m. The equatorial upwelling is quite strong. Beneath the shallow cell, there is almost no net cross equatorial transport above 3,500 m, the equatorial upwelling reaching almost to that depth. Below 4,000 m, the northward flow of bottom water crossing the equator is of the order of 12 Sv.

The MHT maximum divergence (i.e., zero crossing) is located at about 4°N (Fig. 4b). The northern hemisphere maximum is 0.55 PW northward at 20°N. The poleward MHT is greater in the southern hemisphere and reaches its maximum of 1.7 PW at 13°S. The quantitative agreement with Ganachaud and Wunsch (2003) estimates is certainly fortuitous. The discrepancies observed between the advective MHT and the MHT diagnosed from surface fluxes indicate that the Indo-Pacific basin is being cooled between 20 and 60°N (i.e., the North Pacific sector), and between the equator and 10°S (strong cooling). From the equator to 20°N and from 10°S to 35°S, the difference between the two curves of Fig. 4b does not vary with latitude, indicating a quasiequilibrium between the surface flux and the model heat transport.

At global scale, the MHT (Fig. 4c) shows a relatively good symmetry with regard to the equator, a pattern common to estimates obtained from atmospheric analyses (see Trenberth and Caron 2000 for example) with a large

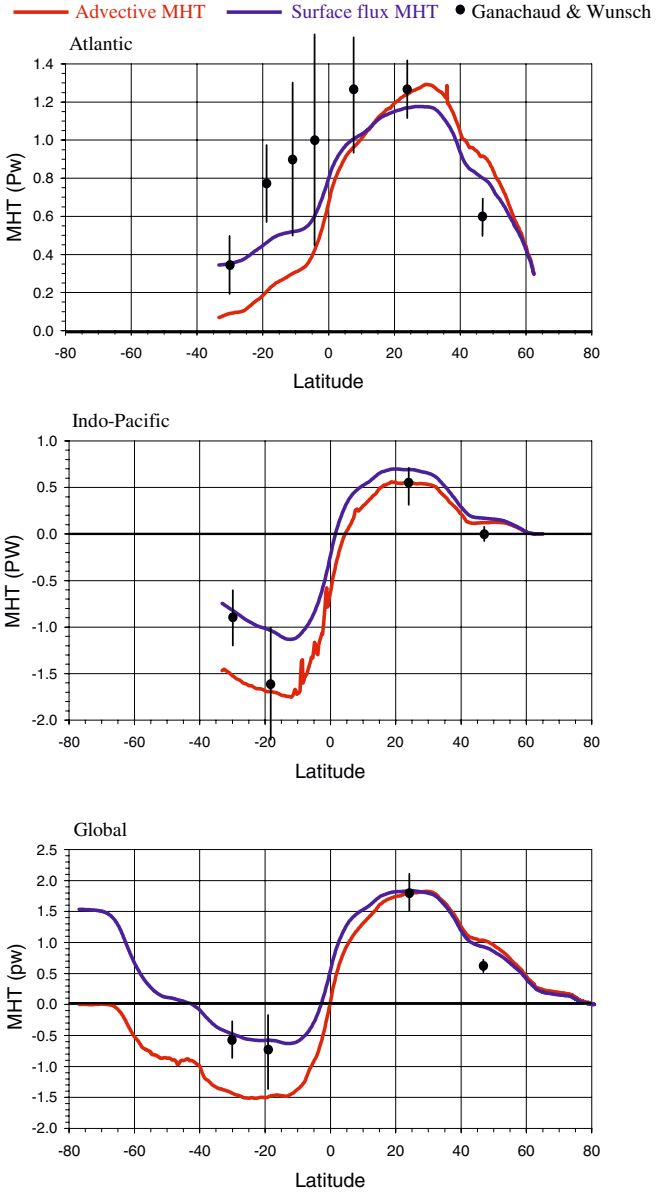

Fig. 4 Meridional heat transport (in PW) averaged over year 8 to 10 of the G22 simulation for the Atlantic, Indo-Pacific, and Global oceans. The advective MHT (*red curve*) is calculated using a 5-day mean model meridional current velocities and temperatures. The surface flux MHT (*blue curve*) is calculated as the meridional integration of surface fluxes. Differences between the *curves* indicate trends and storage. *Black dots* are estimates (with *error bars*) from an inversion of hydrographic data by Ganachaud and Wunsch (2003)

maximum of southward heat transport in the southern hemisphere (1.5 PW at 13°S). Global models usually tend to produce smaller values for the southern hemisphere maximum MHT [for example, 1.2 PW at 12°S in the 1/10 Parallel Ocean Program (POP) model], in agreement with the hydrographic estimate of Ganachaud and Wunsch (2003). Note that an experiment similar to G22 but using a relaxation of SSS to climatological value reduced the southern hemisphere maximum to a value comparable to hydrographic estimates. The sensitivity of MHT to the details of the forcing is thus quite large.

The comparison with the global MHT diagnosed from surface fluxes (Fig. 4c) suggests a quasiequilibrium between heat advection and surface fluxes north of 20°N. In fact, this equilibrium at the global scale is the result of a balance between the warming of the North Atlantic and the cooling of the North Pacific. Between 20°N and 20°S, the global ocean is cooling, the Atlantic providing the major contribution to this cooling from 20°N to the equator, and the contribution of the Indo-Pacific being dominant from the equator to 20°S. The imbalance between both MHT estimates is of the order of 1.0 PW at 60°S, mainly coming from the cooling at tropical latitudes. It will be interesting to see in future sensitivity experiments with different forcing fields how the MHT characteristics presented here are modified.

This brief overview of the model solution indicates that the ORCA-R025 broad circulation patterns correspond to what is expected from a state-of-the-art ocean general circulation model. It also shows that the global meridional circulation, yet too far from steadiness to be quantitatively interpreted, is of very similar strength in all ORCA-R025 simulations compared here, so changes in the MOC intensity between experiments will not be an issue when comparing their respective regional circulation features.

3 Effects of PS and EEN vorticity scheme

We assess the impact of the PS and EEN advection scheme on the model solution by looking at local dynamical circulation features whose spin-up is almost complete after 10 years and whose characteristics should not change significantly (i.e., not to the point of invalidating the conclusions of the present study) during the slow adjustment of the internal thermohaline structure of the ocean to the forcing.

3.1 Global analysis

To identify where the PS and the EEN vorticity scheme produce significant changes in the model solution, we compare the 3-year mean barotropic streamfunction (*BSF*) of simulations G22 and G04 (Fig. 6a). To separate the effects of PS and EEN, we also do this comparison for simulations G03 and G04 (Fig. 6b), both using FS but with only G03 using the EEN scheme (See Table 1). Only changes above 10 Sv are looked at here, which limits our investigation to regions of strong currents (i.e., where the impact of nonlinear terms is strong). The first look at Fig. 6a identifies the region around Antarctica as a region of great impact of the new schemes, the use of which reduces the ACC transport (from 160 to 140 Sv at Drake Passage). This reduction is clearly due to the PS because the map of the BSF differences between the two FS simulations, which only differ by the momentum advection scheme (G03 and G04, Fig. 6b), does not show this pattern. The smaller transport at Drake Passage in G22 (141 Sv compared to 154 Sv in G04) is therefore a consequence of the PS topography. This is consistent with former studies, which demonstrated how crucial the bottom topography is to establish the momentum balance of the ACC (Rintoul et al. 2002; Grezio et al. 2005).

Other regions of great differences are basically the regions of high eke levels shown in Fig. 5: western boundary current systems with the largest impact in the Argentine Basin and the Gulf Stream, the Agulhas Current retroflection region and its extension in the southern Indian ocean, the most intense branches of the ACC in the Indian Ocean sector, and in the Pacific Ocean sector around the Campbell Plateau and beyond. Smaller changes, still significant because they are slightly above 10 Sv, are seen in the Labrador Sea, mainly due to the use of PS as deduced from Fig. 6a,b. This is consistent with the findings of Käse et al. (2001) and Myers (2002) who showed that the use of PS topography strengthened the North Atlantic subpolar gyre. Changes in BSF are also noticeable in the Caribbean Sea and in the east Australian Current.

All the above remarks strongly suggest that the impact of the new schemes is localized where the flow is highly nonlinear and where the topographic constraint is strong, as briefly illustrated in Section 4 (detailed explanation in J. Le Sommer et al. 2005, in preparation). Figure 6a,b indicates that except for the region around Antarctica where the PS topography appears to drive the changes, the EEN advection scheme and PS have comparable contribution.

In the following, we concentrate our analysis on six regions (outlined in Fig. 6a) where changes are particularly large. The impact of PS and EEN on the mean circulation will be assessed by comparing mean sea surface height (*mssh*) and the mean eke of simulation G22 with estimates from observations and from various model experiments. The "observed" mssh used here as reference is the output of the surface drifter and satellite altimetry analysis of Niiler et al. (2003). The observed eke used here as reference is that derived from satellite altimetry by Ducet et al. (2000). Although referred to as observed quantities in the following, we should keep in mind that these are estimates derived from observations and that they have their own inaccuracies and biases generally depending on data coverage (which is quite unequal from a region to another for surface drifters). Model results used are from simulations G04 and G22 performed with the ORCA-R025 model (Table 1) and from simulations carried out with different models: the Ocean Circulation and Climate Advanced Modeling (OCCAM) Project (Webb et al. 1998; Coward and de Cuevas 2005), the POP1/10 model (Maltrud and

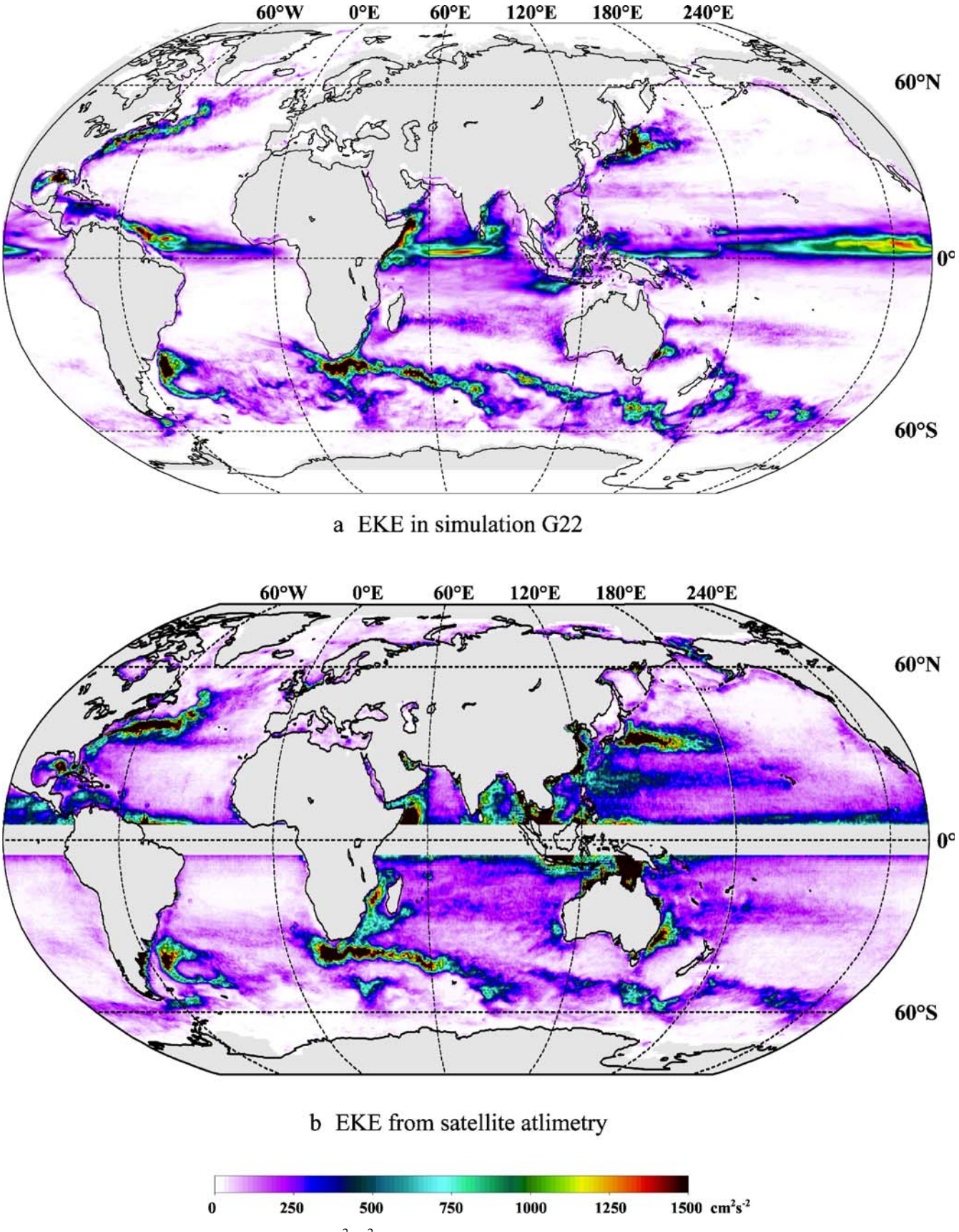

Fig. 5 Global map of eddy kinetic energy (in $cm^2\ s^{-2}$) in simulations G22 (3-year mean) and from satellite altimetry (Topex/Poseidon and ERS; Ducet et al. 2000)

McClean 2005), and the CLIPPER ATL6 model (Penduff et al. 2005). The main characteristics of these latter models are summarized in Table 2. Note that the version of OCCAM uses PS and a large number (66) of vertical levels.

We have to mention here the ocean general circulation model for the earth simulator (OFES). It is a 50-year-long simulation carried out on the Earth Simulator in Japan (Masumoto et al. 2004) with a global implementation of the Modular Ocean Model (MOM)3 code at 1/10° resolution (thus, similar to POP1/10). OFES outputs were not available when we carried out our analyses so this simulation is not included in the present study. However, public Internet access[5] to the OFES 50-year climatological simulation is now available. This simulation uses a PS topography and OFES mean fields could, in future studies, be compared to the POP1/10 solution to assess the impact of the PS at eddy-resolving resolution. We mention some results of this simulation in Section 3.3.

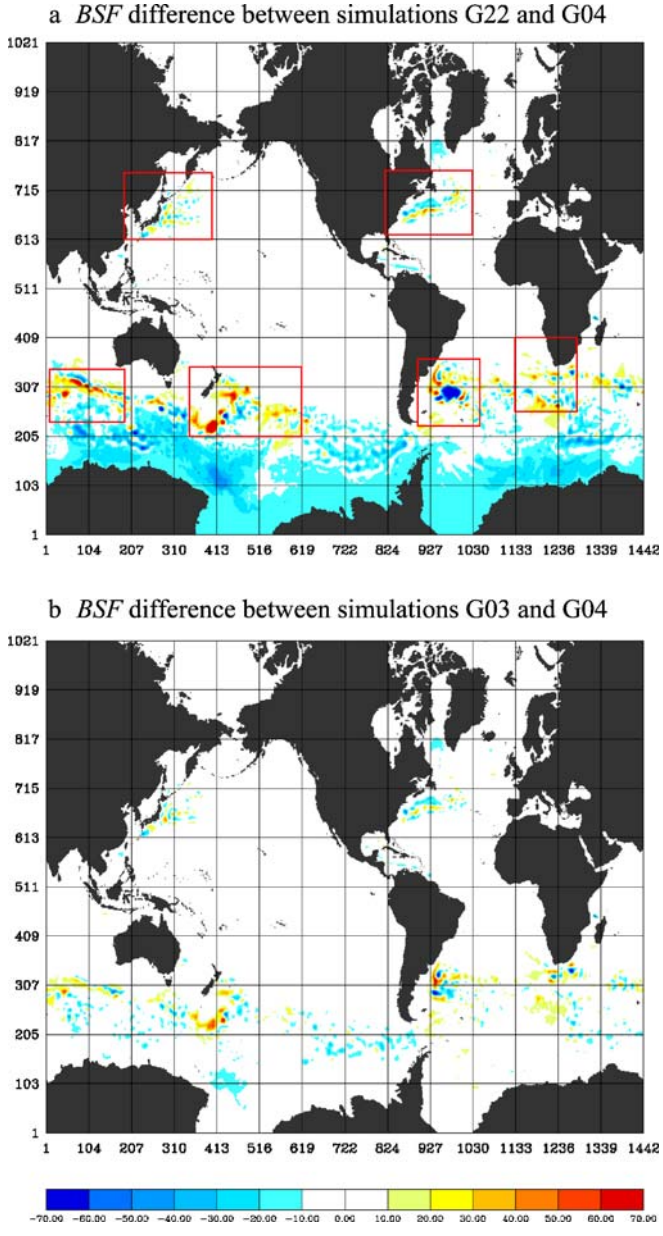

Fig. 6 Difference in the mean barotropic streamfunction (in Sv) between **a** simulations G22 (PS + EEN) and G04 (FS + ENS) indicating where both the partial step topography and EEN scheme play a role, and **b** between G03 (FS + EEN) and G04 (FS + ENS), both full step topography, indicating where advection scheme only has an impact. The *red boxes* identify the regions where model solution is compared to observation and other models. *Color palette* indicates Sv. *Axes* are subdivided by grid point numbers

3.2 The Gulf Stream and North Atlantic Current system

Figure 7 shows several mssh estimates obtained from observations (Fig. 7a) and from various model experiments (Fig. 7b–f). Observed characteristics of the mean path of the Gulf Stream outlined in Fig. 7a are: a clear separation at Cape Hatteras, an elongated anticyclonic southern recirculation cell, the presence of a cyclonic northern recirculation cell indicating the presence of cold slope waters on the Grand Banks, and a crossing of the 40°N line at 60°W. Beyond this point, the path of the North Atlantic Current (NAC) is characterized by a well marked Mann Eddy at 42°N, 43°W and a North West Corner at 50°N, 40°W. Thus, east of 40°W, the path of the NAC is always north of 50°N and follows the topography.

The ORCA-R025 simulation G22 (which includes PS + EEN) reproduces rather well all these features (Fig. 7b), except for the separation of the Gulf Stream, which still shows a slight overshoot and standing inertial oscillations in the current characterized by a standing eddy off Cape Hatteras (the unrealistic *Hatteras eddy*). Nevertheless, the transport of the Hatteras eddy (20 Sv in G22) is significantly reduced compared to the simulation without the new schemes (55 Sv in simulation G04 in Fig. 7d), and even compared to the solutions provided by other models at similar resolution (OCCAM in Fig. 7c) or higher resolution (POP1/10 and ATL6 in Fig. 7e,f). Concerning the other observed characteristics of the Gulf Stream and the NAC, the G22 simulation is by far the most consistent with observations. The path of the mean current in G22 (including the northwest corner and the presence of slope waters) is remarkably accurate for a model of such resolution, despite a weaker Mann Eddy and a stronger mssh gradient between the subtropical and subpolar gyre.

Figure 8 shows several estimates of the eke obtained from satellite altimeter observations (Fig. 8a) and from various model experiments (Fig. 8b–f). In numerical models, the value of this quantity depends on how well the deformation radii are resolved (i.e., on the fact that the model is eddy resolving, like POP1/10, or eddy-permitting, like ORCA-R025 or OCCAM). Therefore, comparing eke levels between models must be moderated by considerations about their differences in resolution. The present analysis gives more attention to the distribution pattern of eke, which reflects the position of the main currents and eddy pathways, rather than comparing values.

[5] http://www2.es.jamstec.go.jp/ofes/eng/index.html.

Table 2 Main characteristics of the 10-year-long sensitivity experiments, G22 and G04, carried out with ORCA-R025, and of the other model simulations compared in this study

Model name	Code	Area	Resolution	Topography	Momentum advection
G22–ORCA-R025	NEMO	Global	1/4°	Partial step	EEN (Arakawa and Lamb 1981)
G04–ORCA-R025	NEMO	Global	1/4°	Full step	ENS (Sadourny 1975)
OCCAM	MOM	Global	1/4°	Partial step	Flux form
POP1/10	POP	Global	1/10°	Full step	Flux form
ATL6	OPA8.1	Atlantic	1/6°	Full step	ENS (Sadourny 1975)

The distribution of eke confirms the improvements due to the PS and the EEN advection scheme to the simulation of the mean currents. Among all 1/4° simulations presented here (G22, G04, and OCCAM), G22 is the one whose eke pattern (Fig. 8b) is the most consistent with observations (Fig. 8a), in particular, along the path of the NAC. Simulation G04, performed with the same model without the new numerical methods, is clearly deficient with regard to the path of the Gulf Stream beyond the Grand Banks. OCCAM shows extremely intense standing eddies at the separation point of the Gulf Stream. The eke pattern in the path of the NAC and the Northwest Corner indicates that this current system is shifted southward, a picture that is usual at this resolution for the MOM. It is interesting to note that models with higher resolution do not perform better in terms of eke distribution pattern. Both POP1/10 and ATL6 show a strong eke maximum at the Gulf Stream separation point and a wide spread of eke east of the Grand Banks. This indicates a misrepresentation of the main path of the NAC. Note, however, that in a regional simulation of the North Atlantic carried out with the POP model at 1/10° resolution by Smith et al. (2000), the path of the Gulf Stream was quite realistic and the distribution of eke was very comparable to the one observed from satellite.

Therefore, the distribution of the eke satellite estimate confirms the picture provided by the observed mssh that the use of PS and EEN advection has considerably reduced the major dynamical biases found in the simulation of the current system of the western North Atlantic by most numerical models.

3.3 Western South Atlantic

Observed and model mssh estimates are shown in Fig. 9 for the western South Atlantic. Improvements due to PS and EEN in the South Atlantic are even more striking than for the North Atlantic, in particular, because the G22 experiment (Fig. 9b) is the only one among all other models to reproduce the high mssh anomaly observed in the center of the Argentinian Basin at 45°W, 45°S (Fig. 9a). This high-pressure pattern is the signature of the standing Zapiola Eddy, first reported from observations by Saunders and King (1995), and clearly seen in float data (Boebel et al. 1999). The first realistic simulation of the Zapiola Eddy was obtained with a sigma coordinate model by de Miranda et al. (1999a) with a resolution of 1/3°. These authors demonstrated that this strong flow pattern, which transports over 100 Sv, is the result of an interaction between the eddies generated in the highly turbulent confluence of the Brazil and the Malvinas currents with the Zapiola drift, a deep depositional topographic feature rising only 1,000 m above the abyssal plain of the Argentinian Basin. In agreement with the theory developed by Dewar (1998), the convergence of the eddy mass flux above the Zapiola drift generates a high pressure above the topography and a large anticyclonic circulation around it. The circulation pattern reaches its equilibrium when the eddy mass flux is balanced by the export of mass in the Ekman bottom boundary layer. de Miranda et al. (1999a) suggested that standard z-coordinate models (i.e., using FS topography) could not simulate this feature because of a poor representation of f/h contours and an increased numerical dissipation due to lateral friction induced by the step-like topography. This has since been confirmed with the ATL6 model simulations (Penduff et al. 2005) and the POP1/10 experiment (Maltrud and McClean 2005), which could not reproduce this first-order feature despite a significantly higher resolution. Our G03 simulation, which includes the EEN vorticity scheme but uses a FS topography (see Table 1), also does not reproduce the Zapiola Eddy. Comparing the BSF differences of Fig. 6 subpanels a and b, it becomes obvious that the use of PS topography is required to simulate this circulation pattern, in agreement with the discussion of de Miranda et al. (1999a).

This requirement may not be sufficient because OCCAM does not reproduce the Zapiola Eddy despite a PS formulation of the topography. A reason could be that the no-slip boundary condition used by default in the MOM code prevents the formation of the anticyclonic circulation, known to be very sensitive to bottom dissipation (de Miranda et al. 1999a). Still, the OCCAM results are contradicted by those of the OFES simulation (Masumoto et al. 2004) because this 1/10° MOM3 global simulation with partial cell topography simulates a well-marked Zapiola Eddy (Sasaki, personal communication). Understanding the behavior of the PS version of the MOM code is likely challenging and certainly deserves a specific investigation.

In addition to the Zapiola Eddy, the representation of the Malvinas and Brazil currents confluence is also significantly improved with PS and EEN (simulation G22, Fig. 9b) when compared to G04. This improvement is also remarkable when compared to solutions produced by the other models, including POP1/10 and ATL6, which used much higher resolutions (1/10 and 1/6°, respectively). G22

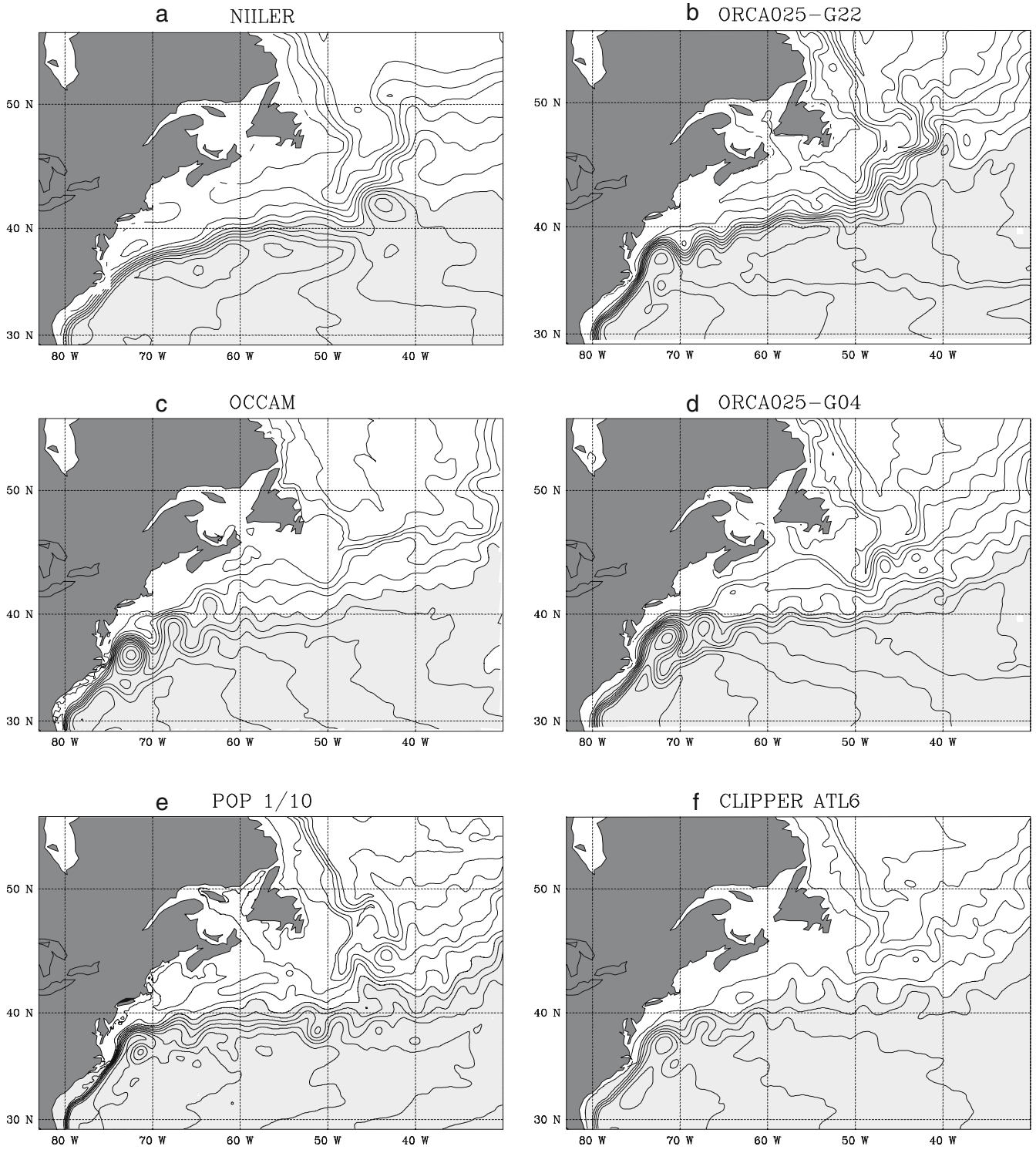

Fig. 7 Estimates of mean sea surface height (*mssh* in cm) in the North Atlantic from **a** observations (Niiler et al. 2003), **b** global ORCA-R025 model simulation G22 (PS + EEN), **c** global OCCAM model simulation, **d** global ORCA-R025 model simulation G04 (FS + ENS), **e** global POP1/10, and **f** Atlantic CLIPPER ATL6 model simulation. All model results present a 3-year mean. To remove mean biases between estimates, the area mean was subtracted for each plot, and thus, *gray* (*white*) areas indicate region of mssh higher (lower) than the area mean. Contour interval is 10 cm

is the only simulation for which the Confluence region is offshore of the Rio de La Plata (36–38°S). In every other simulation, independent of the numerical model used and of resolution, the Confluence region is located beyond 40° S (and as far as 43°S).

The distribution pattern of eke (Fig. 10) confirms this picture. Simulation G22 and Topex/Poseidon exhibit very

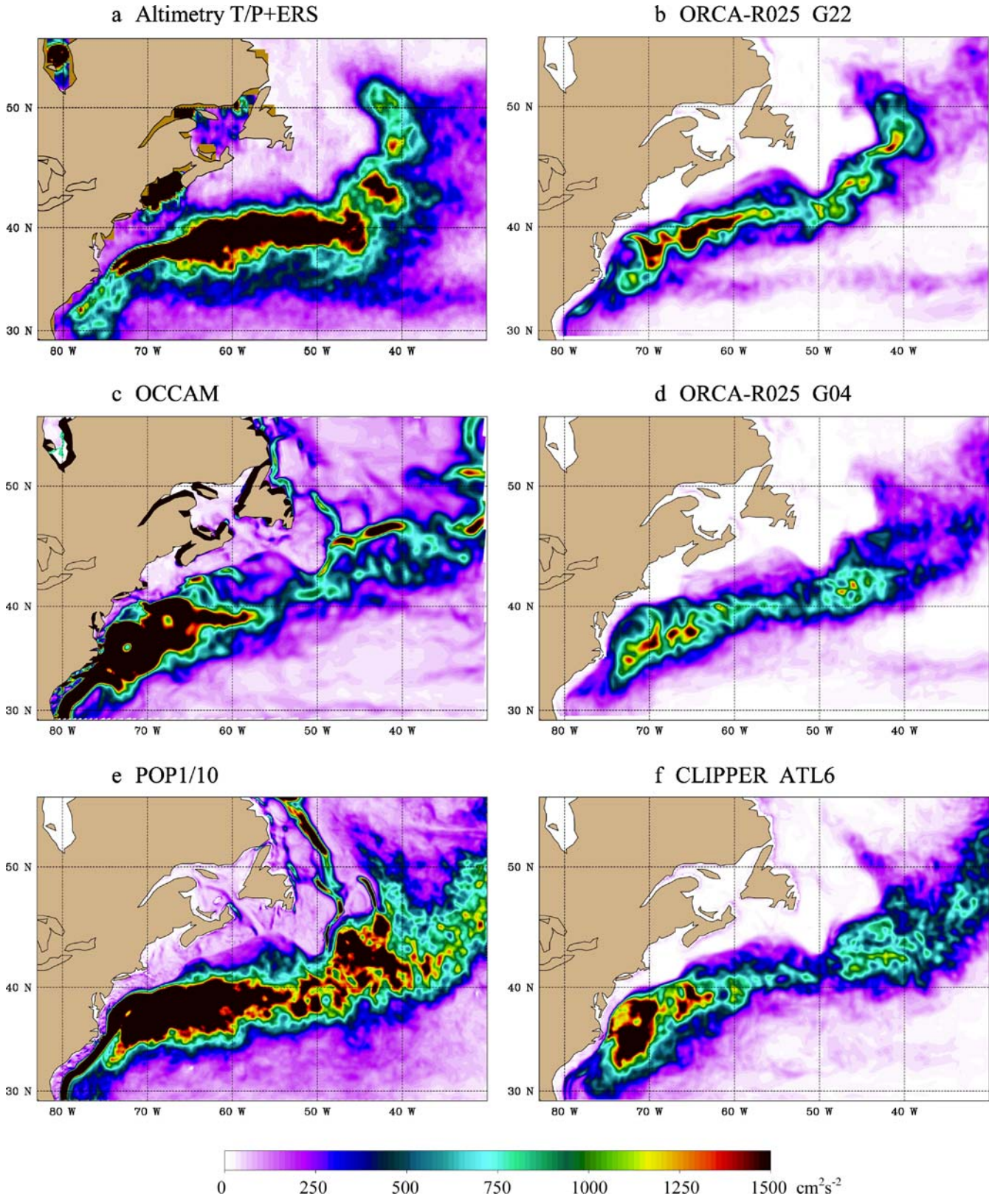

Fig. 8 Estimates of the mean eddy kinetic energy (*eke* in $cm^2\ s^{-2}$) in the North Atlantic from **a** observations (Ducet et al. 2000), **b** global ORCA-R025 model simulation G22 (PS + EEN), **c** global OCCAM model simulation, **d** global ORCA-R025 model simulation G04 (FS + ENS), **e** global POP1/10, and **f** Atlantic CLIPPER ATL6 model simulation. All model results present a 3-year mean

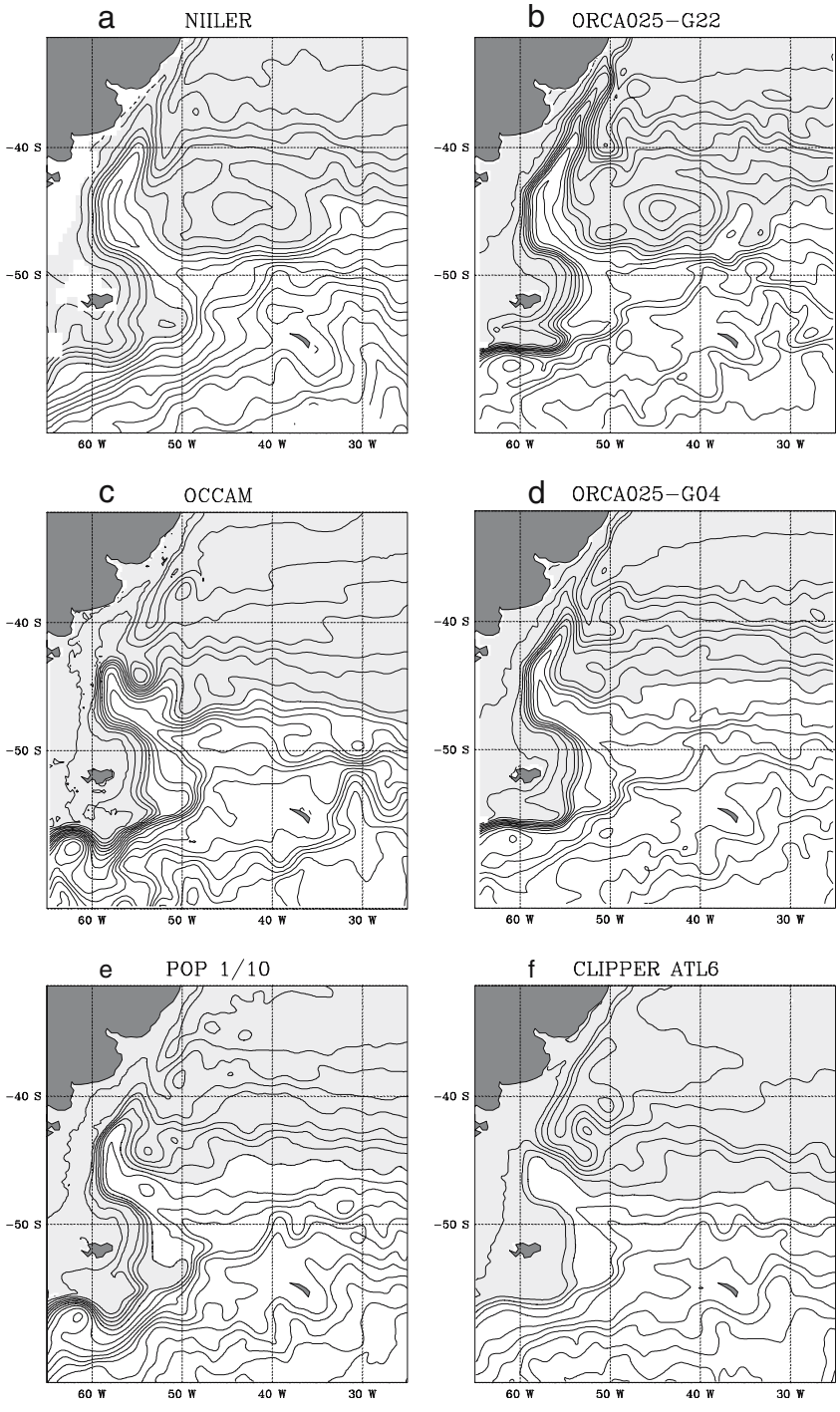

Fig. 9 Same as Fig. 7 (plots of *mssh* in cm) for the western South Atlantic. Contour interval is 10 cm

similar distributions with the characteristic C-shape of high eke levels around the core of the Zapiola Eddy and the small eke levels above. Other models, in particular OCCAM and ATL6, exibit eke patterns characteristic of a strong overshoot to the south of the Brazil Current and no sign of the Zapiola Eddy.

3.4 Cape Basin

The simulation of the Agulhas Current system is also greatly influenced by the new numerical schemes. First, the stability of the Agulhas Current as it flows along South Africa is clearly different in simulations G22 and G04, as illustrated by the snapshots of current speed shown in Fig. 11. When PS and EEN advection are not used (simulation G04, Fig. 11b), the Agulhas Current resembles a train of large eddies rather than a continuous stream as in G22 (Fig. 11a). In G04, the retroflection produces pairs of

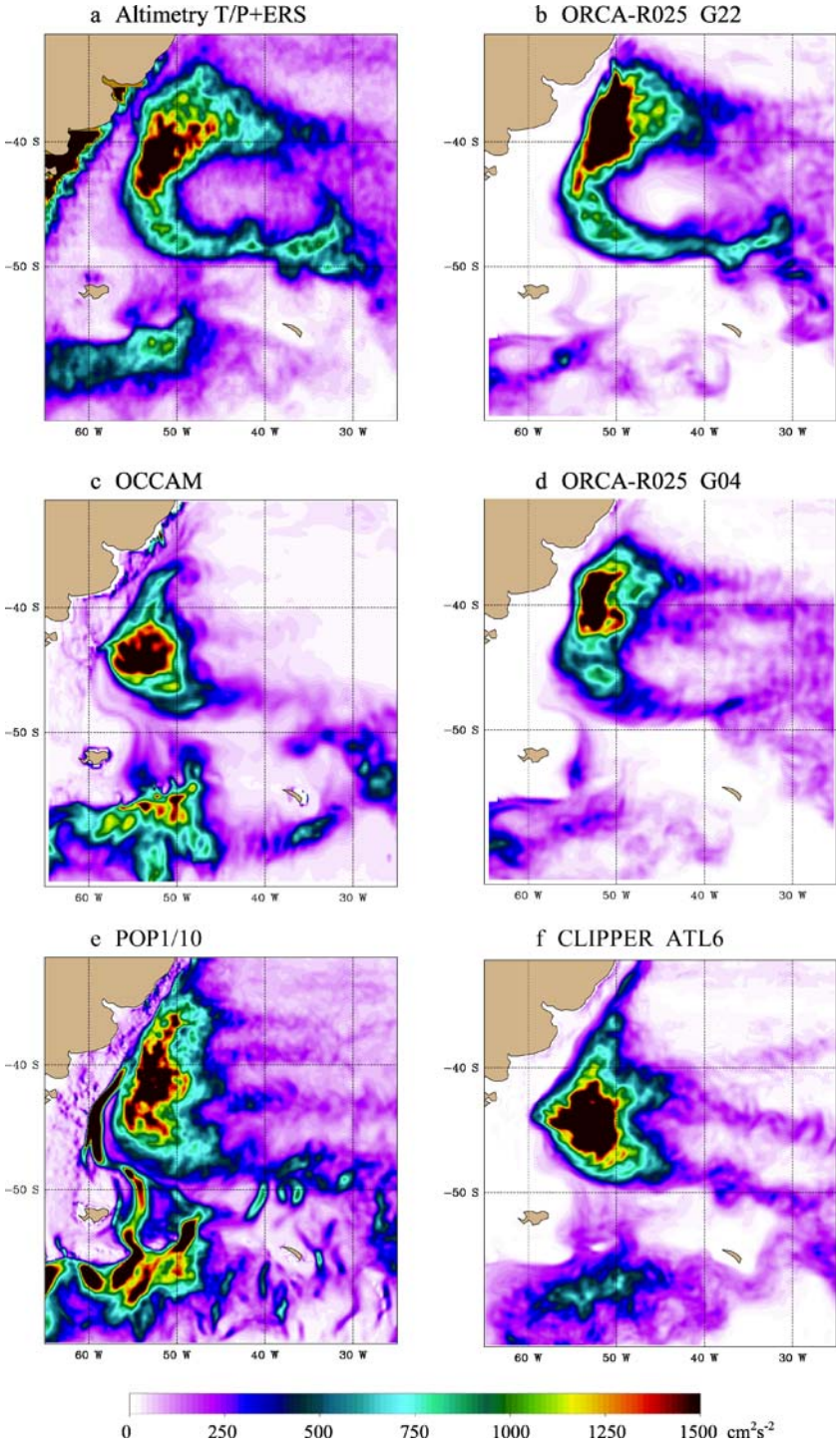

Fig. 10 Same as Fig. 8 (plots of *eke* in $cm^2\ s^{-2}$) for the western South Atlantic

very large eddies (or rings), which later drift into the South Atlantic. The ring generation is very regular in time; rings shed from the retroflection are quite large in size and all use the same pathway to the northwest. Their signature in the distribution of eke (Fig. 12d) is a band of high eke stretching from the retroflection region across the Cape Basin. The ring-generating process is dominated by shear instability. This picture is that usually provided by eddy-permitting numerical models since the Fine Resolution Antarctic Model experiment (Stevens and Killworth 1992) with the very few exceptions of the regional models of Biastoch and Krauss (1999) and de Miranda et al. (1999b), which, although at slightly coarser resolution (1/3°), did not show that bias. In these later regional experiments, the shear instability could be underestimated due to a lack of resolution. Recent models based on the same numerical code from Geophysical Fluid Dynamics Laboratory (OCCAM in Fig. 12c or POP1/10 in Fig. 12e) and on the OPA8.1 code (at 1/3° resolution, Treguier et al. 2001) also present the same type of bias. The ATL6 (1/6°) model

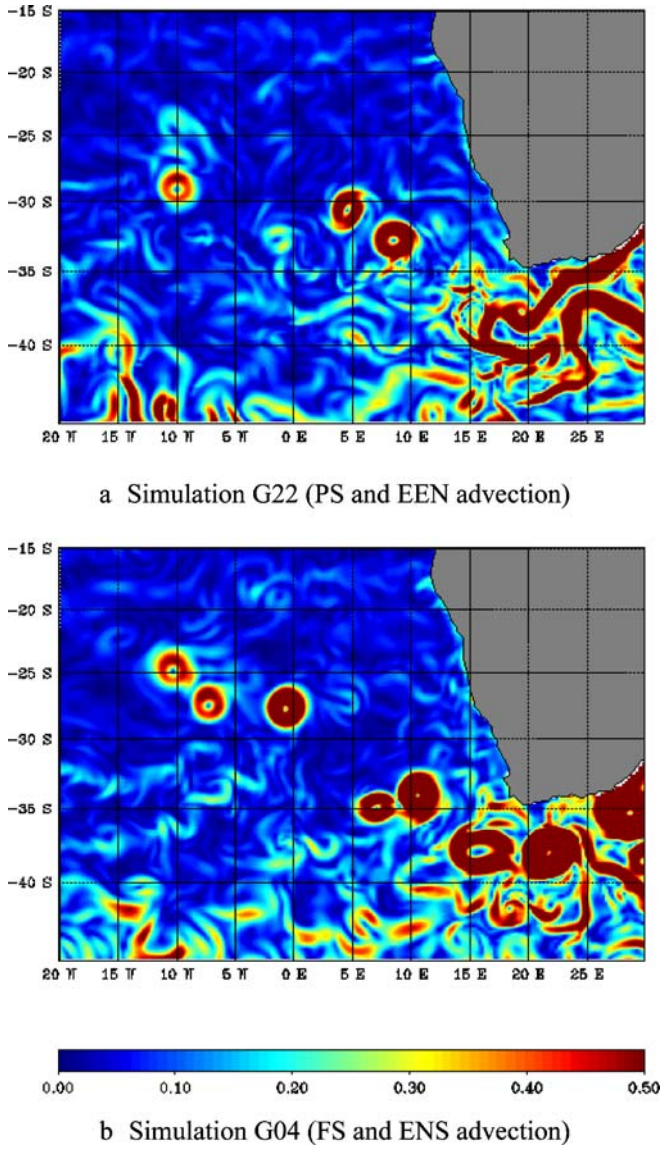

Fig. 11 Snapshot of current speed (in m/s) at 25 m depth in the Cape Basin and the region of the retroflection of the Agulhas Current for **a** simulation ORCA-R025 G22 (PS + EEN) and **b** simulation ORCA-R025 G04 (PS + ENS)

simulations run with OPA8.1 during the CLIPPER project provided a better representation of the Agulhas retroflection region (Treguier et al. 2003). It is possible that the use of a climatological open boundary across 30°E in this later simulation prevented the growth of the inertial eddies seen in Fig. 11b, resulting in a better simulation of the Agulhas Current. Nevertheless, the path of the Agulhas Rings in the South Atlantic was not correctly simulated.

The picture of the circulation in this region provided by simulation G22 with the PS and EEN scheme is significantly different from those described above and is more consistent with observations. In the snapshot of the current speed shown in Fig. 11a, the Agulhas retroflection appears as a large loop of a continuous stream, which extends into the south Atlantic, sometimes as far as 16°E, before it closes and sheds from the main stream. After shedding, this loop breaks into smaller eddies (the Agulhas Rings). Although the above scenario is by far the most frequent during the 10 years of the G22 simulation, we noticed a few periods when the Agulhas Current behaved in a way similar to that observed in G04. But overall, the eddy field in G22 is more chaotic than in G04, the Agulhas Rings rarely produced by pair and their path across the South Atlantic not as regular. We expect to reach a more complete understanding of the model behavior with the longer interannual forcing experiment of the Common Ocean-ice Reference Experiment (50 years) that will be performed in the near future.

Discrepancies noted above regarding the generation and pathway of the Agulhas Rings have drastic consequences on the Cape Basin eke distribution shown in Fig. 12. The eke pattern of simulation G22 (Fig. 12b) is by far the most consistent with that provided by satellite altimetry (Fig. 12a), although a tendency for a preferred path of the eddies in their westward drift still remains. As in satellite observations, largest eke values in G22 are found in the retroflection loop and in the returning Agulhas Current. In the other model simulations, quite large eke values are also found along the east African coast (i.e., in the Agulhas Current before the retroflection loop) and in the path of the rings in the South Atlantic—features not found in the Topex/Poseidon data. Maps of mssh (not shown) show a main path of the returning Agulhas Current along the northern flank of the Agulhas Plateau in simulation G22, very similar to that of the observed mssh of Niiler et al. (2003). This explains the "pinching" of the eke pattern at 25°E, 39°S, high eke levels being found at the north side of the plateau in the mean current, and minimum eke levels being found on the plateau itself. The other models do not show such pinching of the eke pattern at the Agulhas Plateau, which suggests that the G22 simulation is more realistic in accounting for the effects of topography on the mean flow.

3.5 Kuroshio

The simulation of the mean position of the Kuroshio along the coast of Japan is improved by the new schemes. The comparison of the mssh simulated by experiments G22 (Fig. 13b) and G04 (Fig. 13c) shows that G22 is again closer to the observations (Fig. 13a). In this latter simulation, location and meandering of the main stream along the Ryukyu Archipelago and southern Japan (i.e., before the current separates from the coast of Japan) compare very well with observations. The separation is marked by a slight overshoot with two standing eddies aligned offshore, and the path of the mean current is shifted 1°N of the observed position. Without PS and EEN advection (simulation G04), the overshoot and the mean current location are shifted even more to the north, and the standing eddies are now aligned along the coast reaching beyond 40°N. This is reflected in the pattern of the BSF difference of Fig. 6a, which shows negative values (i.e., reduced transport) on the north side along the Kuroshio

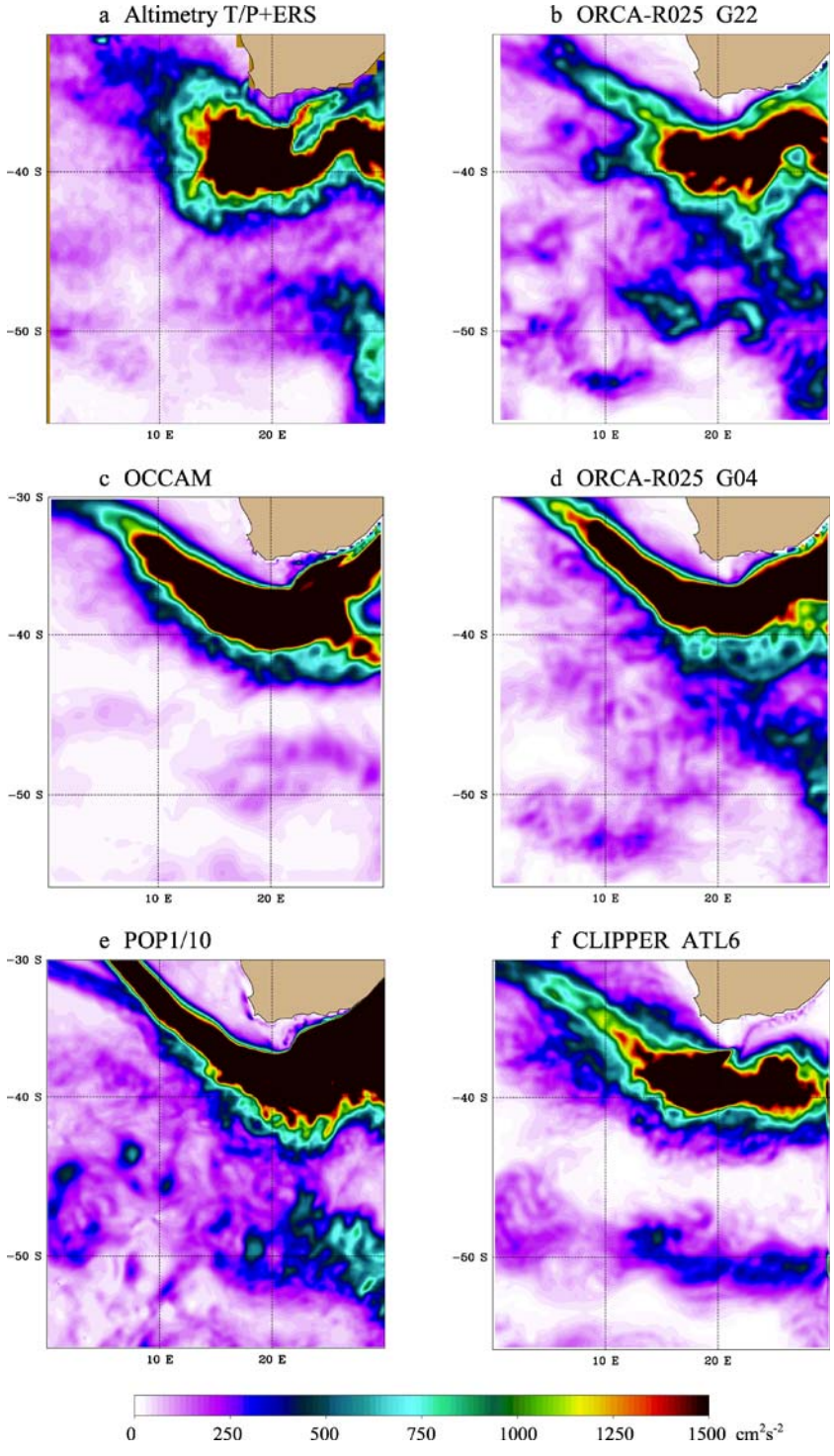

Fig. 12 Same as Fig. 8 (plots of *eke* in $cm^2\ s^{-2}$) for the Cape Basin in the South Atlantic

extension and positive values (i.e., increased transport) on the south side. This indicates a southward shift of the mean current path in simulation G22 compared to G04. The path of the Kuroshio after its separates from Japan is better located in POP1/10 (but not in OCCAM), but the intense high/low dipole of mssh south of Japan (also seen in OCCAM, Fig. 13c,e) is in strong disagreement with observations.

Eke shows a significant reduction in the Kuroshio extension in simulation G22 (Fig. 5a). In the observations, high eke levels are found much farther to the east (see Fig. 5b). POP1/10 (no figure shown, see Maltrud and McClean 2005) simulates a rather realistic eastward extension of eke in the North Pacific Ocean, indicating that simulating this feature could be more a resolution issue than a current topography interaction issue.

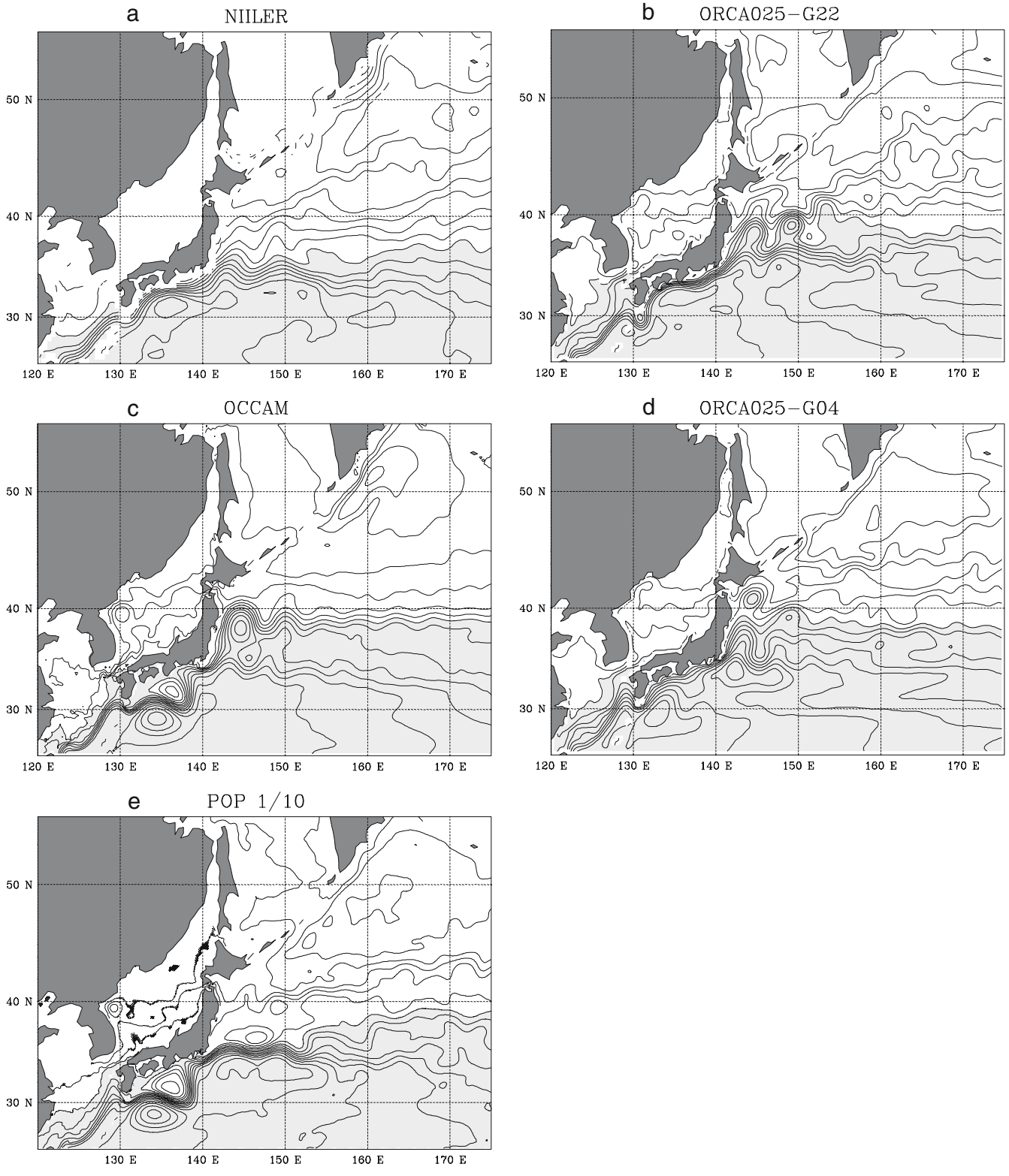

Fig. 13 Same as in Fig. 7 (plots of *mssh* in cm) for the western Pacific (without the CLIPPER model, which only covers the Atlantic). Contour interval is 10 cm

3.6 South Indian Ocean

The south Indian Ocean (the red box to the southwest of Australia in Fig. 6a) is another region where the BSF difference between simulations G22 and G04 shows a pattern indicating a meridional shift of the mean current. The bottom topography of the region (Fig. 15) is characterized by the Kerguelen Plateau in the southwest

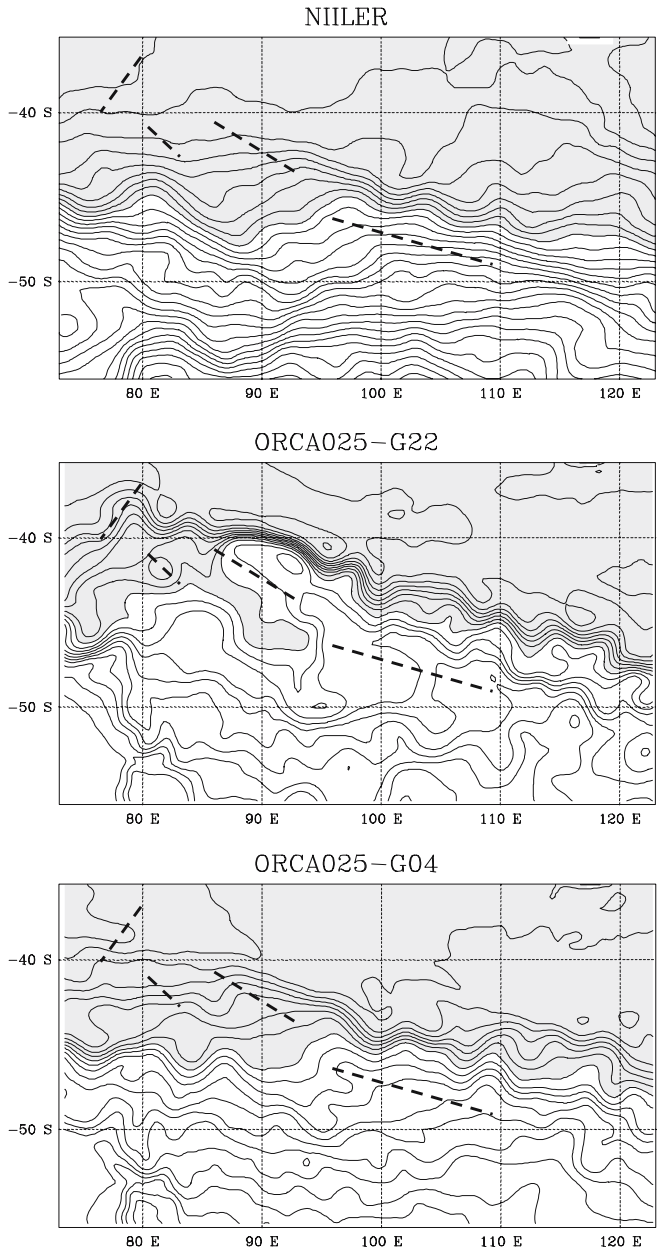

Fig. 14 Estimates of mean sea surface height (*mssh* in cm) in the South Indian Ocean from (*top*) observations (Niiler et al. 2003), (*middle*) global ORCA-R025 model simulation G22 (PS + EEN), and (*bottom*) global ORCA-R025 model simulation G04 (FS + ENS). All model results present a 3-year mean. Mean biases between estimates were removed by subtracting the area mean for each plot. Thus, *gray* (*white*) areas indicate region of mssh higher (lower) than the area mean. Contour interval is 10 cm. The *bold dashed lines* indicate the location of the main topographic features of the South Indian Ridge as reported in the topography map of Fig. 15

corner of the domain and the Amsterdam Island in the northwest corner at 41°S, 78°E from where the Southeast Indian Ridge (SIR) stretches to the southeast. The passage between the islands of Kerguelen and Amsterdam at 75°E features a rise of the bottom topography of 1,500 m above the abyssal plains of the western and eastern Indian basins, and is likely to influence the path of the ACC to the east.

The observed flow in the area can be described from the mssh of Niiler et al. (2003) shown in Fig. 14 and the eke distribution obtained from Topex/Poseidon (Fig. 15). The ACC enters this region passing between Kerguelen and Amsterdam as a broad current spreading between 45 and 50°S. In its eastward route, the main stream of the ACC makes a large meander at 80°E while the topography rises slightly between the Kerguelen–Amterdam passage. Further down stream, the ACC crosses the SIR between 90 and 100° E. It then tilts southeastward to flow along the northern flank of the ridge. The ACC shows significant eke levels as it passes the Kerguelen Plateau (between 70 and 90°E) and after crossing the ridge (from 105 to 120°E, Fig. 15a). This circulation scheme is very consistent with that recently deduced from autonomous floats drifting at 900 mb (Davis 2005), suggesting a significant barotropic component of the flow.

The mssh in simulation G04 (no PS and EEN advection) exhibits a similar behavior to the observed one, the ACC crossing the SIR at the same location (Figs. 14c and 15c). OCCAM and POP1/10 simulations (no figure shown) are very similar to G04. However, both these models tend to produce more zonal flows and to show less sensitivity to the bottom topography. This is well illustrated by their respective eke patterns (Fig. 15c,e), which do not exhibit the observed tilt according to the orientation of the SIR.

In contrast to the observed estimate, the mssh in simulation G22 reveals a strong topographic influence and a significant branching of the ACC (Fig. 14b). At the entrance of the domain (75°E) the main stream of the ACC is split in two branches. One branch, not present in the observed mssh, flows north up to Amsterdam Island where it crosses the SIR. It continues to flow southeastward along the northern side of the ridge and significantly intensifies, probably by topographic influence between 80 and 100°E. The other branch, which enters the domain along the eastern Kerguelen Plateau, behaves in a way similar to the observed mssh. The flow meanders eastward, part of it crossing the SIR in the same passage as suggested by the observed mssh between 90 and 100°E. The northward split of the ACC at the longitude of the Kerguelen Plateau is not related to PS alone (although its contribution is dominant). Simulation G03, which uses the FS topography and the new EEN scheme, already differs from G04 (Fig. 6b) and also shows this split of the ACC path (no figure shown).

The circulation branches described above correspond to regions of high eke (Fig. 15). The high eke values seen in G22 on the northern side of the SIR in the (80°E, 100°E) longitude band (Fig. 15b) is the direct result of the instability of the northern branch of the ACC. In the eastern part of the domain (100°E, 120°E), the eke is rather similar in pattern between G22, G04, and the estimate derived from altimeter observations; high eke values are found on the north side of the SIR aligned along the topography.

Considering the remarkably good agreement of G22 with observations in most regions, this unrealistic behavior of the ACC in this longitude band is rather disconcerting. It is likely that the behavior of the northern branch and, in particular, the intensification of the current by the strong

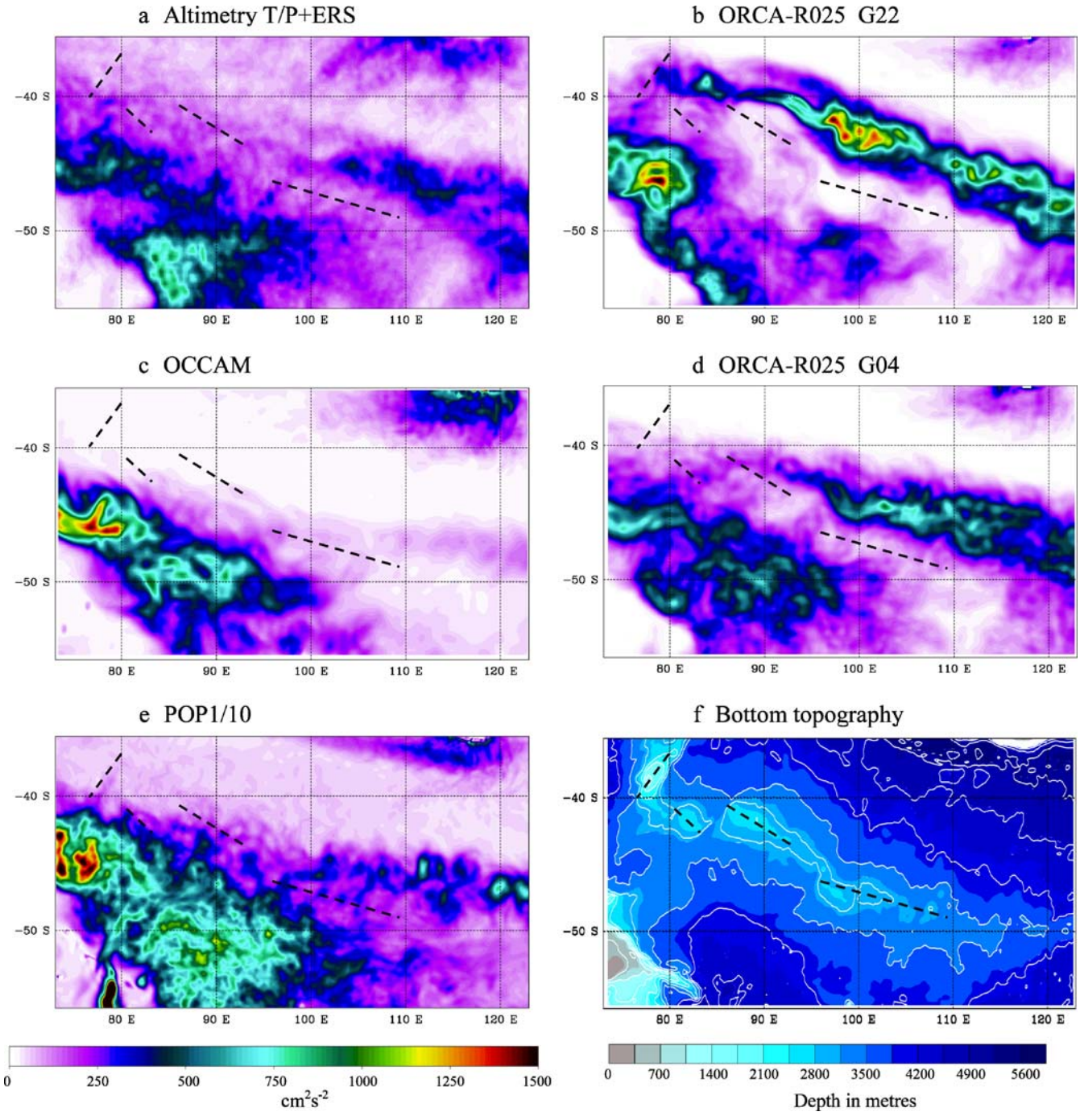

Fig. 15 Same as in Fig. 8 (plots of *eke* in $cm^2\ s^{-2}$) for the South Indian Ocean (without the CLIPPER model, which only covers the Atlantic). The bottom topography of the area is shown (*bottom right plot*) with a contour interval of 500 m. The *bold dashed lines* indicate the location of the main topographic features of the South Indian Ridge

topography of Amsterdam Island and the SIR is the downstream consequence of the splitting of the ACC as it reaches the longitude of the Kerguelen Plateau. This split, which seems to be related to the topographic slopes and its relation to the use of the PS and EEN numerical schemes deserves a more detailed investigation.

The difference between the G22 and G04 simulations may be partly explained by the differences between the PS and the FS representations of the topography of the Kerguelen–Amsterdam passage. Because the bottom depth is adjusted to the local *z*-level in the FS topography, a flat channel exists in G04, which connects the western and eastern abyssal plains at the depth of 3,530 m (the 37th level of the model). This channel does not exist in the original Etopo2 topography nor in the PS topography, which both have a sill in the passage at the depth of nearly 3,300 m. The existence of this channel in G04 may

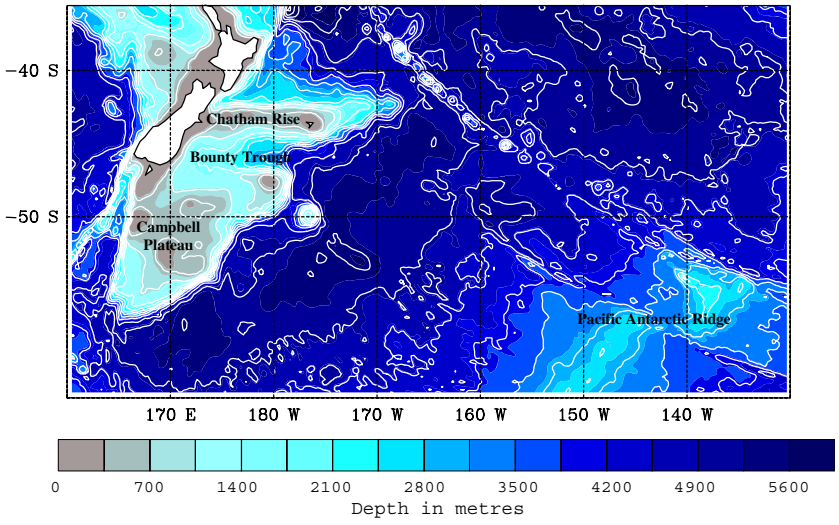

Fig. 16 Bottom topography (in meters) of the South Pacific around New Zealand. *Colors* indicate the depth. Contour interval is 500 m

influence the path of the ACC between the islands, which may thus agree with observations for the wrong reasons.

3.7 Campbell Plateau

The region south and west of New Zealand is also characterized by large changes in BSF due to the use of both PS and EEN (Fig. 6). Major BSF changes between G22 and G04 are localized along the topography of the Campbell Plateau and the Chatham Rise (see the bottom topography map in Fig. 16). Figure 17 shows the various estimates of mssh. As noted for most regions we have already looked at, there is a remarkable agreement between the observed mssh and that simulated in G22, the latter showing currents at finer scale. Every circulation feature, like the branching of the ACC at the tip of the Campbell Plateau (55°S, 165°E), the trapping of the ACC on the slope of the east side of the Campbell Plateau, the well-marked anticyclonic circulation far inside the Bounty Trough (reaching the coast of New Zealand and flowing out the trough along Chatham Rise), are reproduced. Even farther to the west (between 150 and 130°W), the model reproduces the ACC splitting into two branches while it crosses the Pacific Antarctic Ridge. The G04 simulation, although rather realistic in this region, does not show the same amount of details. In particular, flows trapped on topographic slopes are weaker. However, one could wonder whether the G22 could overemphasize the topographic constraint, as suggested for the South Indian region. This will have to be investigated in the future with additional in situ data and by looking at the baroclinic structure of the flow. Note that recent subsurface float observations presented by Davis (2005, Fig. 3) show a very consistent circulation inside Bounty Trough, trapped on the topographic slope, very much like the circulation pattern simulated in G22. OCCAM and POP1/10 models do not simulate the flow with similar details despite similar or higher resolution. In particular, the intrusion of the ACC into the Bounty Trough is not reproduced. An interesting model feature is the standing cyclonic eddy found in the abyssal plain south of the Campbell Plateau at 55°S, 172°E. This feature is seen in every model and corresponds in the observed mssh to a "flat" (i.e., no gradient) mssh, separating two branches of the ACC. Models and observations are thus consistent, indicating that the mean flow does not go through but around the abyssal plain.

4 Discussion and conclusion

We have provided an overview of progress in modeling the ocean general circulation at eddy-permitting (1/4°) resolution achieved within the European project DRAKKAR. The main focus was on modeling issues whose importance was continuously emphasized by Christian Le Provost, which are the numerical treatment of nonlinearities and bottom topography. We introduced this paper with a brief presentation of the DRAKKAR community project, the birth of which Christian Le Provost actively participated. We have described the eddy-permitting, global 1/4° resolution, model configuration implemented by the project ORCA-R025. This ocean/sea-ice general circulation model uses the NEMO code, which is a new version of the OPA primitive equation, *z*-level, ocean circulation model coupled to the LIM2 sea-ice model. The characteristic of the new code, which is evaluated here, lies in a new advection scheme for momentum equations (the EEN scheme) and the use of a PS representation of the bottom topography. Ten-year-long sensitivity simulations with and without EEN and PS numerics were run with ORCA-R025 under a climatological atmospheric forcing. The impact of the new numerical choices on the model solution were assessed by comparing the model mssh and eke with their equivalent in the observations and with other state-of-the-art model simulations at equivalent or higher resolution.

Although our analysis remained quite descriptive, it demonstrated that the combination of the EEN scheme with PS yields a remarkable improvement in the major circulation patterns. Well-known biases in the representation of

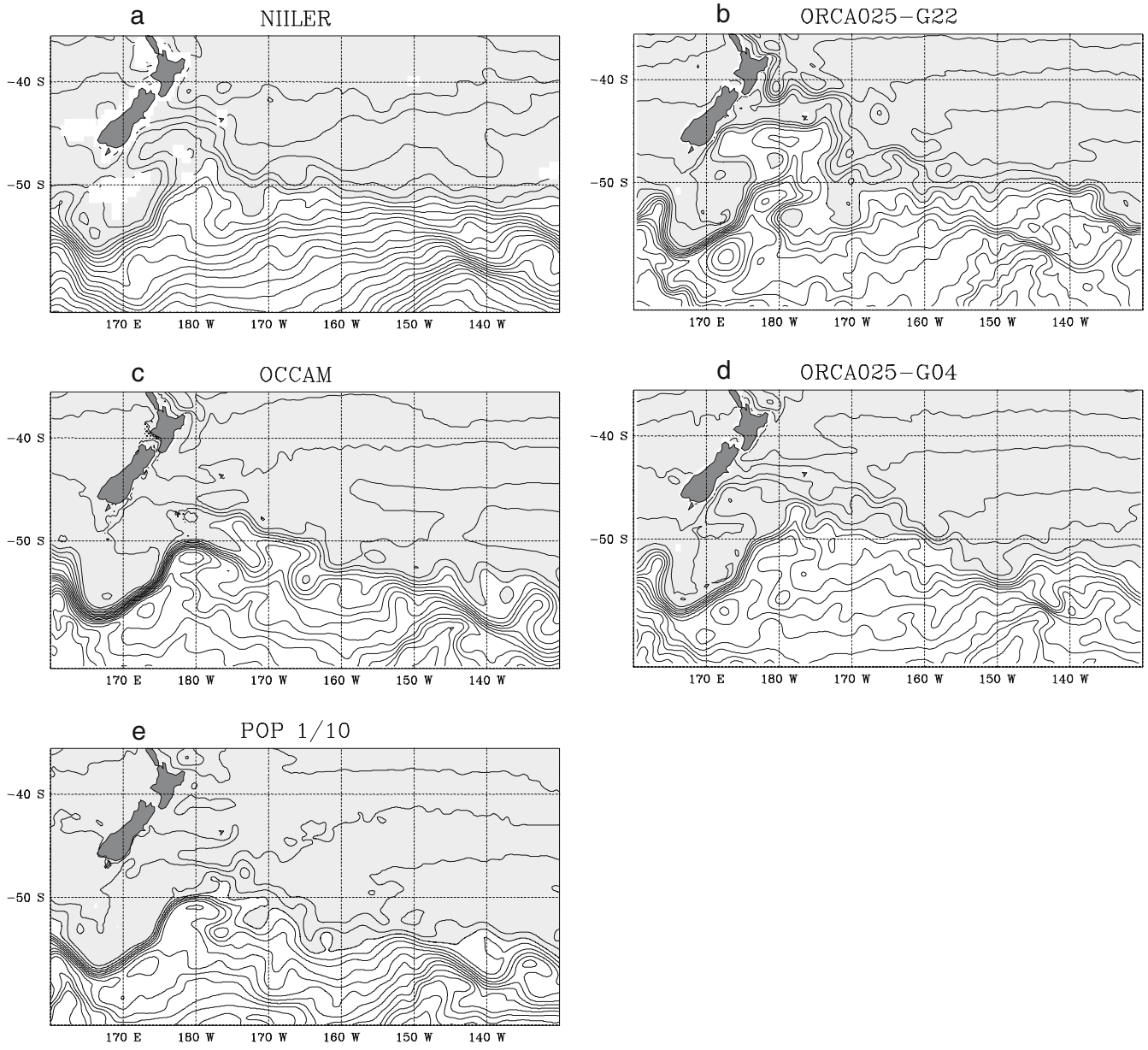

Fig. 17 Same as in Fig. 7 (plots of *mssh* in cm) for the Campbell Plateau in the South Pacific (without the CLIPPER model, which only covers the Atlantic). Contour interval is 10 cm

western boundary currents, such as in the Atlantic, the separation of the Gulf Stream, the path of the North Atlantic Current at the Northwest Corner, the location of the Brazil–Malvinas Confluence, and the strength of the Zapiola Eddy, are significantly corrected. Similar improvements are found in the Pacific, Indian, and Southern Oceans, and characteristics of the simulated mean circulation patterns are generally much closer to observations. In comparison with other models at similar resolution (the 1/4° OCCAM), the ORCA-R025 configuration generally performs better. In addition, the ORCA-R025 solution is often comparable to (or even better than) solutions obtained at 1/6° (CLIPPER model) or 1/10° (POP Model) resolution in some aspects concerning mean flow patterns and distribution of eke. Note that the improvements in mssh and eke presented here generally correspond to improvements in the deep circulation (not discussed in this paper) and, in particular, in a stronger and quite coherent deep western boundary current.

The impact of the new numerical schemes is not a uniformly positive one. The flow pattern of the ACC in the South Indian Ocean is different from that suggested by both mssh and eke observations when PS and EEN are used. Moreover, the solution with this later combination seems degraded when compared to the solution with the FS topography and the former ENS advection, although this could be due to compensating errors in the FS representation of topography. The unrealistic branching of the ACC at the longitude of the Kerguelen plateau (Section 3.6) suggests a strong local sensitivity of the model solution

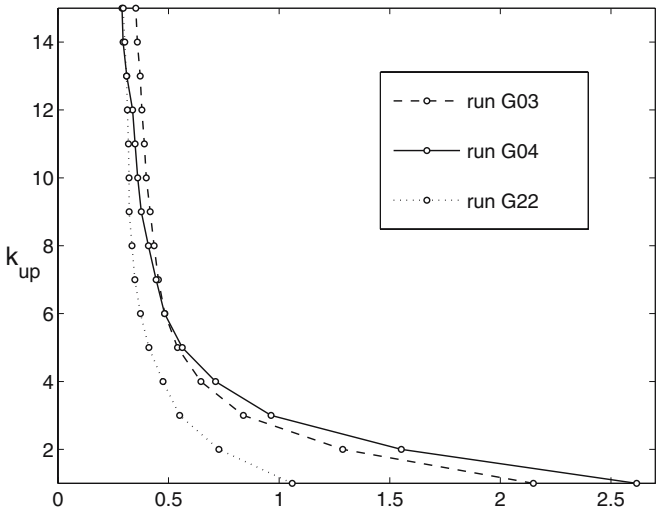

Fig. 18 Snapshot of the normalized grid scale irregularities in vertical velocity fields as a function of the level above the bottom (k^{up}), averaged over the Gulf Stream area in simulations G04 (FS + ENS), G03 (FS + EEN), and G22 (PS + EEN). The difference (δw) between the vertical velocity (w) and its nine cell average ($\overline{w}$) was computed on each model level. The vertical levels were reindexed from the bottom ($k^{up}=i$ is the ith level above the bottom). The grid scale irregularity, which is plotted, is the ratio between the averages at constant k^{up} of $|\delta w|$ and $|\overline{w}|$.

to the bottom topography, which we do not understand yet. Additional simulations, driven by different atmospheric forcing, produced a MOC and an ACC of different strength from G22 but still presented a similar flaw in the region, and the same happened with a different algorithm to calculate the pressure gradient between partial cells. Additional simulations are underway, but at present, we are not able to explain this local behavior of the solution.

The use of PS topography and EEN advection scheme thus dramatically affects the ORCA-R025 model solution in regions, which are subject to strong current–topography interactions. Understanding in full the dynamical origin of these improvements is beyond the scope of the present paper, but first analyses point to the presence of small-scale noise near the bottom as a crucial factor. Figure 18 shows a measure of the vertical velocity noise (the deviation of the vertical velocity from its nine-point average) in the Gulf Stream region as a function of depth (a similar picture is obtained in all regions of the global model). In all three cases (G03, G04, and G22), we find this noise to increase significantly toward the bottom. Near the bottom layer (approximately eight levels up from the bottom), the noise is drastically reduced by the use of the EEN scheme in combination with PS topography (G22). According to J. Le Sommer et al. (2006, in preparation), it is plausible that the noise level has time–mean effects through the diffusion of momentum and tracer, and that the choice of bottom cell and advection schemes consequently affects the vertical energy distribution near sloping topography and thereby the larger scale flow.

We conclude that significant corrections of the mean biases seen in general circulation model solutions at eddy-permitting resolution, which were not obtained by increasing resolution, were obtained by changing the numerical methods used. Studies searching for a full understanding of the impact of the EEN and PS numerics on the model dynamical solution are currently under way. It was already shown that the impact of the EEN scheme is greatest at grid cells nearest a side wall (J. Le Sommer et al. 2006, in preparation), suggesting a great sensitivity of the momentum advection to the lateral and bottom boundary condition. The numerical treatment of momentum advection has somewhat been overlooked in global and climate ocean models, except perhaps for the dynamics of the Equatorial Undercurrent. This contrasts with numerous studies dealing with the importance of advection schemes for temperature, salinity and other tracers (see, for example, Lévy et al. 2001). It also contrasts with the Regional Oceanic Modeling System where special effort was put into developing new advection schemes for momentum (Shchepetkin and McWilliams 2005).

In recent years, improvement of global ocean models was sought through an increase in horizontal resolution, and global model simulations were performed at 1/10 and 1/12° resolutions (Maltrud and McClean 2005; Kara et al. 2005; Coward and de Cuevas 2005). Our results bring forward a different view and point out the numerical treatment of momentum advection and bottom topography and, more generally, the improvement of the model numerics as an issue of prime importance for eddy-permitting climate modeling.

But eddy-permitting models were shown to perform worse than coarse resolution models in the representation of important small-scale processes such as the restratification after a deep convection event (J. Chanut et al. 2006, submitted for publication; Czeschel 2005) or the deep overflows. It is clear that physical parameterizations developed at coarse resolution (for example, the "bolus velocity" of Gent and McWillams 1990 or the "bottom boundary layer" of Beckmann and Döscher 1997) are not suited for that resolution. It is likely that development or adaptation of parameterizations of these key subgrid scale processes at eddy-permitting resolution should be coordinated with the development of numerics because their efficiency could depend on the model numerical schemes.

The complexity of the global ice–ocean system is such that the sensitivity of an eddy-permitting model is still poorly known. Nevertheless, it is expected that many ocean models used for climate prediction, which provide our only means to assess future changes, will begin to operate in the eddy-permitting regime within a few years. Hence, developing an improved understanding of how this regime plays a key role in controlling global ocean dynamics has become a high priority.

Acknowledgements This work is a contribution of the DRAKKAR project. Support to DRAKKAR comes from various grants and programs listed hereafter. French national programs GMMC, PATOM, and PNEDC. PICS 2475 from Institut National des Sciences de l'Univers (INSU) and Centre National de la Recherche Scientifique (CNRS). Kiel SFB460 and CLIVAR-marin (03F0377A/B) supported by Deutsche Forschungsgemeinschaft. European integrated project MERSEA. Computations presented in this study were performed at Institut du Développement et des Ressources en Informatique Scientifique (IDRIS). Finally, we would like to thank P. Niiler, N. A. Maximenko, and J. C. McWilliams who kindly made their data sets available from the Web.

References

Adcroft A, Hill C, Marshall J (1997) Representation of topography by shaved cells in a height coordinate ocean model. Mon Weather Rev 125:2293–2315

Arakawa A, Lamb VR (1981) A potential enstrophy and energy conserving scheme for the shallow water equations. Mon Weather Rev 109:18–36

Barnier B, Le Provost C (1993) Influence of bottom topography roughness on the jet and inertial recirculation of a mid-latitude gyre. Dyn Atmos Oceans 18:29–65

Beckmann A, Döscher R (1997) A method for improved representation of dense water spreading over topography in geopotential-coordinate models. J Phys Oceanogr 27:581–591

Berliand ME, Strokina TG (1980) Global distribution of the total amount of clouds. Hydrometeorological, Leningrad, p 71 (in Russian)

Biastoch A, Krauss W (1999) The role of mesoscale eddies in the source regions of the Agulhas current. J Phys Oceanogr 29:2303–2317

Blanke B, Delecluse P (1993) Variability of the tropical Atlantic Ocean simulated by a general circulation model with two different mixed-layer physics. J Phys Oceanogr 23:1363–1388

Blayo E, Le Provost C (1993) Performance of the capacitance matrix method for solving Helmholtz type equations in ocean modelling. J Comp Physiol 104:347–360

Boebel O, Davis RE, Ollitrault M, Peterson RG, Richardson PL, Schmid C, Zenk W (1999) The intermediate depth circulation of the western South Atlantic. Geophys Res Lett 26(21):3329–3332

Böning CW, Bryan FO (1996) Large-scale transport processes in high resolution circulation models. In: Borntraeger G (ed) The warm watersphere of the North Atlantic. Berlin, pp 91–128

Böning CW, Rhein M, Dengg MJ, Dorow C (2003) Modeling CFC inventories and formation rates of Labrador Sea Water. Geophys Res Lett 30(2):1050. DOI 10.1029/2002GL014855

Bryan FO, Holland WR (1989) A high resolution model of the wind- and thermohaline-driven circulation in the North Atlantic Ocean. In: Muller P, Henderson D (eds) Aha Huliko'a parameterization of small-scale processes. Hawaii Institute of Geophysics, Hawaii, pp 99–115

CERSAT (2002) Mean wind fields (MWF product), vol. 1. In: ERS-1, ERS-2 & NSCAT user manual. Ref C2-MUT-W-05-IF, version 1.0

Coward AC, de Cuevas BA (2005) The OCCAM 66 level model: model description, physics, initial conditions and external forcing. Southampton Oceanography Centre internal document 99, Southampton, UK, p 83

Czeschel L (2005) The role of eddies for the deep water formation in the Labrador Sea. Ph.D. thesis, Kiel University, Institut f. Meereswissenschaften, p 101

de Miranda A, Barnier B, Dewar WK (1999a) On the dynamics of the Zapiola anticyclone. J Geophys Res Ocean 104:21137–21149

de Miranda A, Barnier B, Dewar WK (1999b) Mode waters and subduction rates in a high resolution South Atlantic simulation. J Mar Res 57:213–244

Davis ER (2005) Intermediate-depth circulation of the Indian and South Pacific Oceans measured by autonomous floats. J Phys Oceanogr 35:683–707

Dewar WK (1998) Topographic and barotropic transport control by bottom friction. J Mar Res 56:295–328

Ducet N, Le Traon PY, Reverdin G (2000) Global high resolution mapping of ocean circulation from Topex/Poseidon and ERS-1 and -2. J Geophys Res Ocean 105(C8):19477–19498

DYNAMO Group (1997) DYNAMO: dynamics of the North Atlantic models: simulation and assimilation with high resolution models. Ber Institute für Meereskunde, Universität Kiel, pp 294–334

Fichefet T, Morales Maqueda MA (1997) Sensitivity of a global sea ice model to the treatment of ice thermodynamics and dynamics. J Geophys Res 102:12609–12646

Ganachaud A, Wunsch C (2003) Large-scale ocean heat and freshwater transports during the World Ocean Circulation Experiment. J Climate 16:696–705

Gent PR, McWillams JC (1990) Isopycnal mixing in ocean circulation models. J Phys Oceanogr 20:150–155

Goosse H (1997) Modeling the large scale behaviour of the coupled ocean–sea ice system. Ph.D. thesis, Université Catholique de Louvain, Louvain-la-Neuve, Belgium, p 231

Grezio A, Wells NC, Ivchenko VO, de Cuevas BA (2005) Dynamical budgets of the Antarctic Circumpolar Current using ocean general-circulation models. Q J Roy Meteor Soc Part A 607(28):833–860

Jakobsson M, Cherkis NZ, Woodward J, Macnab R, Coakley B (2000) New grid of arctic bathymetry aids scientists and mapmakers. Eos Trans Am Geophys Union 81(9):89, 93, 96

Jourdan D, Balopoulos E, Garcia-Fernandez MJ, Maillard C (1998) Objective analysis of temperature and salinity historical data set over the Mediterranean Basin. IEEE Press, Piscataway, NJ

Kalnay E, Kanamitsu M, Kistler R, Collins W, Deaven D, Gandin L, Iredell M, Saha S, White G, Woollen J, Zhu Y, Chelliah M, Ebisuzaki W, Higgins W, Janowiak J, Mo KC, Ropelewski C, Leetmaa A, Reynolds R, Jenne R (1996) The NCEP/NCAR 40-year reanalysis project. BAMS 77:437–471

Kara AB, Barron CN, Martin PJ, Smedstad LF, Rhodes RC (2005) Validation of interannual simulations from the 1/8° global Navy Coastal Ocean Model. Ocean Model 11:376–398

Käse RH, Biastoch A, Stammer DB (2001) On the mid depth circulation in the Labrador and Irminger seas. Geophys Res Lett 28:3433–3436

Lee MM, Coward AC (2003) Eddy mass transport in an eddy-permitting global ocean model. Ocean Model 5/3:249–266

Levitus S, Boyer TP, Conkright ME, O'Brian T, Antonov J, Stephens C, Stathopolos L, Johnson D, Gelfeld R (1998) World ocean database 1998. NOAA Atlas NESDID 18, US Government Printing Office, Washington, DC

Lévy M, Estublier A, Madec G (2001) Choice of an advection scheme for biogeochemical models. Geophys Res Lett 28 (19):3725–3728. DOI 10.1029/2001GL012947

Lythe MB, Vaughan DG (2001) BEDMAP: a new ice thickness and subglacial topographic model of Antarctica. J Geophys Res Solid Earth 106:11335–11351

Madec G, Imbard M (1996) A global ocean mesh to overcome the North Pole singularity. Climate Dyn 12:381–388

Madec G, Delecluse P, Imbard M, Levy C (1998) OPA 8.1 general circulation model reference manual. Notes de l'IPSL, Université P. et M. Curie, B102 T15-E5, 4 place Jussieu, Paris cedex 5, No. 11, p 91

Maltrud ME, McClean JL (2005) An eddy resolving global 1/10° ocean simulation. Ocean Model 8:31–54

Maltrud ME, Smith RD, Semtner AJ, Malone RC (1998) Global eddy-resolving ocean simulations driven by 1985–1995 atmospheric fields. J Geophys Res Ocean 103:30825–30853

Masumoto Y, Sasaki H, Kagimoto T, Komori N, Ishida A, Sasai T, Miyama T, Motoi T, Mitsudera H, Takahashi K, Sakuma H, Yamagata T (2004) A fifty-year eddy-resolving simulation of the world ocean: preliminary outcomes of OFES (OGCM for the Earth Simulator). J Earth Simulator 1:35–56

Myers PG (2002) SPOM: a regional model of the sub-polar North Atlantic. Atmos-Ocean 445–463
Murray RJ (1996) Explicit generation of orthogonal grids for ocean models. J Comput Phys 126:251–273
Niiler PP, Maximenko NA, McWilliams JC (2003) Dynamically balanced absolute sea level of the global ocean derived from near-surface velocity observations. Geophys Res Lett 30 (22):2164. DOI 10.1029/2003GL018628
Pacanowski RC, Gnanadesikan A (1998) Transient response in a z-level ocean model that resolves topography with partial cells. Mon Weather Rev 126:3248–3270
Penduff T, Barnier B, Verron J, Kerbiriou MA (2002) How topographic smoothing contributes to differentiating the eddy flows simulated by sigma- and z-level models. J Phys Oceanogr 32:122–137
Penduff T, Barnier B, Molines J-M, Madec G (2005) On the use of current meter data to assess the realism of ocean model simulations. Ocean Model 11(3–4):399–416
Rintoul SR, Hughes CW, Olbers D (2002) The Antarctic Circumpolar Current system. In: Siedler G, Church J, Gould J (eds) Ocean circulation and climate, international geophysics series, vol. 77. Academic, New York
Roullet G, Madec G (2000) Salt conservation, free surface and varying volume: a new formulation for ocean GCMs. J Geophys Res 105:23927–23942
Sadourny R (1975) The dynamics of finite-difference models of the shallow-water equations. J Atmos Sci 32(4):680–689
Saunders PM, King BA (1995) Bottom currents derived from a ship borne ADCP on the WOCE cruise A11 in the South Atlantic. J Phys Oceanogr 25:329–347
Shchepetkin AF, McWilliams JC (2005) Regional ocean model system: a split–explicit ocean model with a free surface and topography—following vertical coordinate. Ocean Model 9:347–404
Smith WHF, Sandwell DT (1997) Global sea-floor topography from satellite altimetry and ship depth soundings. Science 277:1956–1962
Smith RD, Maltrud ME, Bryan FO, Hecht MW (2000) Numerical simulation of the North Atlantic Ocean at 1/10°. J Phys Oceanogr 30:1532–1561
Steele M, Morley R, Ermold W (2001) PHC: a global ocean hydrography with a high quality Arctic Ocean. J Climate 14:2079–2087
Stevens DP, Killworth PD (1992) The distribution of kinetic energy in the Southern Ocean. A comparison between observations and an eddy-resolving general circulation model. Phil Trans Royal Soc B 338:251–257
Timmmerman A, Goosse H, Madec G, Fichefet T, Ethe C, Dulière V (2005) On the representation of high latitude processes in the ORCA-LIM global coupled sea-ice ocean model. Ocean Model 8:175–201
Treguier AM, Reynaud T, Pichevin T, Barnier B, Molines JM, de Miranda A, Messager C, Beismann JO, Madec G, Grima N, Imbard M, Le Provost C (1999) The CLIPPER project: high resolution modelling of the Atlantic. Int WOCE Newsl 36:3–5
Treguier AM, Barnier B, de Miranda A, Molines JM, Grima N, Imbard M, Madec G, Messager C, Michel S (2001) An eddy permitting model of the Atlantic circulation: evaluating open boundary conditions. J Geophys Res 106:22115–22129
Treguier AM, Boebel O, Barnier B, Madec G (2003) Agulhas eddy fluxes in a 1/6° Atlantic model. Deep-Sea Res Part 2 Top Stud Oceanogr 50:251–280
Trenberth KE, Caron JM (2000) Estimates of meridional atmosphere and ocean heat transports. J Climate 14:3433–3443
Trenberth KE, Olson JG, Large WG (1989) A global ocean wind stress climatology based on ECMWF analyses. National Center for Atmospheric Research, boulder, NCAR/TN-338+STR, p 93
Verron J, Le Provost C (1985) A numerical study of quasi-geostrophic flow over isolated topography. J Fluid Mech 154:231–252
Verron J, Le Provost C, Holland WR (1987) On the Effects of a midocean ridge on the general circulation: numerical simulations with an eddy-resolved ocean model. J Phys Oceanogr 17:301–312
Webb D J, de Cuevas BA, Coward AC (1998) The first main run of the OCCAM global ocean model. Internal document no. 34, Southampton Oceanography Centre, UK
Willebrand J, Barnier B, Böning C, Dieterich C, Killworth PD, Le Provost C, Jia Y, Molines JM, New AL (2001) Circulation characteristics in three eddy-permitting models of the North Atlantic. Prog Oceanogr 48:123–162
Xie P, Arkin PA (1997) Global precipitation: a 17-year monthly analysis based on gauge observations, satellite estimates, and numerical model outputs. Bull Am Meteorol Soc 78 (11):2539–2558